

# Dynamic landscape of protein occupancy across the *Escherichia coli* chromosome

5 Peter L. Freddolino<sup>1,2,\*</sup>, Haley M. Amemiya<sup>3</sup>, Thomas J. Goss<sup>1</sup>, and Saeed Tavazoie<sup>4,5,6,\*</sup>

1: Department of Biological Chemistry, University of Michigan Medical School, Ann Arbor, MI, USA

10 2: Department of Computational Medicine and Bioinformatics, University of Michigan Medical School, Ann Arbor, MI, USA

3: Cellular and Molecular Biology Program, University of Michigan Medical School, Ann Arbor, MI, USA

4: Department of Biological Sciences, Columbia University, New York, NY, USA

5: Department of Systems Biology, Columbia University, New York, NY, USA

15 6: Department of Biochemistry and Molecular Biophysics, Columbia University, New York, NY, USA

\*: To whom correspondence should be addressed. Email: [petefred@umich.edu](mailto:petefred@umich.edu), [st2744@columbia.edu](mailto:st2744@columbia.edu)

20

## Abstract

Free-living bacteria adapt to environmental change by reprogramming gene expression through precise interactions of hundreds of DNA-binding proteins. A predictive understanding of bacterial physiology requires us to globally monitor all such protein-DNA interactions across a range of environmental and genetic perturbations. Here, we show that such global observations are possible using an optimized version of *in vivo* protein occupancy display technology (IPOD-HR), and present a pilot application to *E. coli*. We observe that the *E. coli* protein-DNA interactome organizes into two distinct prototypic features: (1) highly dynamic condition-dependent transcription factor occupancy, and (2) robust kilobase scale occupancy by nucleoid factors, forming silencing domains analogous to eukaryotic heterochromatin. We show that occupancy dynamics across a range of conditions can rapidly reveal the global transcriptional regulatory organization of a bacterium. Beyond discovery of previously hidden regulatory logic, we show that these observations can be utilized to computationally determine sequence-specificity models for the majority of active transcription factors. Our study demonstrates that global observations of protein occupancy combined with statistical inference can rapidly and systematically reveal the transcriptional regulatory and structural features of a bacterial genome. This capacity is particularly crucial for non-model bacteria which are not amenable to routine genetic manipulation.

25  
30  
35

## 40 Introduction

Transcriptional regulation plays a central role in establishing adaptive gene expression states. In bacteria, the dominant regulators are transcription factors (TFs) [1,2] and sigma factors, which direct the activity of RNA polymerase holoenzyme to a specific subset of promoters [3,4]. The phenotypic state of the bacterial cell is determined in large part by its transcriptional regulatory state which, in turn, is dictated by the binding pattern of TFs and sigma factors across the chromosome, likely in interplay with structural factors such as the local supercoiling state [5].

At present, however, our knowledge of the complete wiring of bacterial transcriptional regulatory networks remains insufficient to fully predict or design regulatory responses to arbitrary environmental conditions. The case of *Escherichia coli* serves as an illustrative case study: due to its status as a pre-eminent model organism and important human pathogen, the *E. coli* transcriptional regulatory network has been an intense subject of investigation for several decades. As a result, researchers have obtained an increasingly comprehensive and detailed map of the binding specificities and physiological roles of transcriptional regulators in this organism [6]. However, roughly one quarter of the ~250 transcription factors in *E. coli* have no available binding or regulatory data [7], and many more are virtual unknowns in terms of the signals that might alter their regulatory activity. Likely as a result of this knowledge gap, Larsen and colleagues recently found that despite our broad knowledge of the potential regulatory targets of *E. coli* transcription factors, our ability to predict regulatory behavior on the basis of expression levels of transcription factors is no better than it would be for random networks. The authors attribute this partly to the fact that even when a TF is expressed, in many cases it will not bind its targets in the absence of additional signals [8]. Furthermore, *E. coli* represents a best-case scenario in terms of our knowledge state for a bacterial transcriptional regulatory network, and for most bacterial species current databases lag far behind.

Expanding our capability to predict, and ultimately design, bacterial regulatory responses will be critical for controlling bacterial pathogenesis and engineering synthetic microbes in biotechnology applications. Achieving such a complete predictive understanding, however, requires substantial additional information both on the binding sites of as-yet uncharacterized TFs, and the actual physical occupancy of sites for both known and uncharacterized factors across conditions. Widely used methods such as ChIP-seq pose difficulties on both fronts: they demand a combinatorial explosion of experiments to study many transcription factors across a variety of conditions, and require either an antibody against each TF of interest or genetic manipulation sufficient to add an epitope tag to each target TF.

In order to significantly advance our understanding of transcriptional network dynamics and chromosomal structure, we sought to monitor, in parallel, the occupancy states of all DNA-binding proteins across a set of genetic and environmental perturbations. We argue that such comprehensive observations are critical for defining the global modes of transcriptional regulation and determining the regulatory logic that underlies adaptive reprogramming of gene expression, particularly given the importance of combinatorial logic by many factors and sites in dictating transcriptional output [9]. In order to achieve our goal, we decided to employ the

concept of *in vivo* protein occupancy display (IPOD) which we, in a previous proof-of-concept study, demonstrated to reveal global occupancy of protein binding sites across the *E. coli* chromosome [10]. However, we had to introduce critical modifications and enhancements in order to deconvolve distinct contributions from sequence-specific TFs and RNA-polymerase and define binding sites at high-resolution. We will refer to this second generation IPOD technology as IPOD-HR (*in vivo* protein occupancy display - high resolution). IPOD-HR enables efficient coverage of a large range of physiological conditions in relatively few experiments (one experiment per condition, rather than the one experiment per TF per condition that would be required for ChIP-seq). As we demonstrate below, a single IPOD-HR experiment can reveal the occupancy dynamics of dozens of known and novel active TFs genome-wide, permitting rapid profiling of global transcriptional regulatory logic across different conditions. Furthermore, the comprehensive nature of IPOD-HR profiles enables efficient statistical inference of sequence specificity models (TFBS motifs) for active transcription factors, both recapitulating well-known regulatory logic and revealing the presence and condition-dependent activities of novel regulatory elements.

Here, we characterized the dynamics of the global protein-DNA interactome of *E. coli* across a range of three physiological conditions and three genetic perturbations. Our observations allowed us to infer, in parallel, the activities of most annotated transcription factors across conditions, and provided a catalogue of many additional likely regulatory sites and DNA sequence motifs for uncharacterized TFs. With the compact set of experiments, we reveal the dramatic regulatory dynamics of dozens of transcription factors that collectively shape the response of *E. coli* to changing environments. In sharp contrast, we find that at the kilobase scale, the genome is characterized by a set of relatively static structural domains, which consist of transcriptionally silent loci with dense protein occupancy that appear mostly constitutive across a range of physiological conditions. These regions, which we refer to as EPODs (extended protein occupancy domains) following the nomenclature of Vora *et al.* [10], appear to act, at least partially, to suppress prophages and mobile genetic elements.

Because our approach does not rely on prior knowledge of TFs of interest or genetic manipulation of the target organism, but rather only on essential physico-chemical properties of protein-DNA complexes, we expect that it will be broadly applicable across bacterial species, even those which cannot be cultured or genetically manipulated. Our approach lays the technical and analytic foundation to rapidly characterize the regulatory and structural features of any bacterial chromosomes.

## Results

### Global high-resolution profiling of condition-dependent transcription factor occupancy across the *E. coli* chromosome

The IPOD-HR procedure is shown in schematic form in **Figure 1A**: cells are grown under a physiological condition of interest, fixed using formaldehyde, and then lysed. Heavy digestion of

125 the chromosomal DNA provides minimized DNA fragments that may be in either a protein bound or unbound state. The protein bound DNA fragments are subsequently isolated using a phenol-chloroform extraction. Under appropriate buffer conditions, the amphipathic protein-DNA complexes are depleted from the aqueous phase and partition to a robust disc at the aqueous-organic interface [10].

130 As we will demonstrate below, the measurements enabled by IPOD-HR can subsequently be used for a broad range of downstream analyses, such as simultaneous monitoring of the activities of characterized TFs, large-scale inference of binding motifs for previously uncharacterized DNA-binding proteins, and identification of key occupancy sites driving previously unrecognized gene regulatory logic. To accomplish these objectives, it is essential to separate out the occupancy signal of RNA polymerase from that of specific regulatory factors of interest. Otherwise, the strong occupancy signal caused by RNA polymerase could mask changes in protein occupancy that in fact provide regulatory information. To deconvolve occupancy caused by sequence-specific TFs and that of RNA polymerase, we subtract the normalized RNA polymerase ChIP-seq signal from that of the normalized raw IPOD-HR signal (see Methods for details), generating a corrected IPOD-HR profile that is a more precise representation of the cell's dynamic regulatory state (**Fig. 1B**). IPOD-HR is conceptually similar to the original IPOD method [10] in terms of overall workflow, but contains critical optimizations and extensions designed to permit genome-wide identification of binding by TFs and organizing factors such as nucleoid-associated proteins in a condition-specific manner. On the experimental end, IPOD-HR incorporates a more stringent washing procedure (the inclusion of a Tris base wash and an additional interphase extraction step to increase the specificity of isolation of protein-DNA complexes), as well as pretreatment of the cells with rifampin prior to crosslinking to minimize the contributions of RNA polymerase occupancy to the observed signal, and an RNA polymerase ChIP-seq experiment in parallel to allow separation of RNA polymerase occupancy from that of other proteins. On the computational end, IPOD-HR makes use of a completely re-written analysis pipeline (as detailed in Methods) that provides proper adjustment for RNA polymerase occupancy, gives an integrated workflow for calculation of total protein occupancy (including uncertainty estimates), and allows for the identification of key occupancy features such as occupancy peaks corresponding to individual binding sites, as well as large regions of high protein occupancy that act as silencing complexes on the *E. coli* genome.

160 We note in passing that, at first glance, IPOD may seem to share superficial similarities with FAIRE (formaldehyde-assisted isolation of regulatory elements, originally described in [11]). However, FAIRE experiments were designed to detect regions of nucleosome-depleted DNA in eukaryotic chromosomes. IPOD was independently developed to detect occupancy of individual factors in prokaryotic chromosomes [10], and IPOD-HR contains further optimizations and additional experimental and computational steps to improve performance in detecting both localized and large-scale protein occupancy in bacteria.

165 An illustrative example of the ability of IPOD-HR to identify regulatory protein occupancy, its dynamics across conditions, and the importance of factoring out the RNA polymerase signal, is

shown in **Figure 1C**. We consider the IPOD-HR occupancy profiles for the promoter region upstream of the *purC* gene in wild type (WT) and  $\Delta purR$  cells during growth in rich defined medium (RDM). Based on the characterized behavior of PurR (which binds DNA in response to exogenous purine supplementation [12,13]), under this growth condition, transcription of *purC* should be repressed by binding of PurR to its promoter. However, if one considers only the raw IPOD-HR occupancy profiles (top panel), binding to the PurR site in this region is apparent in both WT and  $\Delta purR$  cells. The resolution to this seeming paradox becomes apparent through inclusion of the correction for RNA polymerase occupancy (middle panel), which is substantially higher in  $\Delta purR$  cells. As expected, the resulting corrected IPOD-HR occupancy profiles (bottom panel) reveal a protein occupancy peak directly on top of the annotated PurR binding site in this region in the WT cells, and no detectable occupancy in the  $\Delta purR$  cells. This demonstrates the ability of IPOD-HR to reveal condition-dependent TF occupancy dynamics even in regions that may overlap with RNA polymerase binding. In the following sections, IPOD-HR refers to the RNA polymerase-corrected occupancy signal, unless otherwise noted.

## Local and large-scale protein occupancy patterns across the *E. coli* chromosome

To benchmark our ability to quantitatively profile protein occupancy at high spatial resolution, we performed IPOD-HR on *E. coli* cells from mid-exponential growth in rich defined medium (**Fig. 2A**). Over the length of the chromosome we observed a large number of small peaks, presumably corresponding to protein binding events at individual regulatory sites. In addition, we observed many large-scale (> 1 Kb) regions of high occupancy which we refer to as extended protein occupancy domains (EPODs), following the nomenclature of Vora et al. [10]. An example of condition-dependent changes in binding of local TFs is shown in **Fig. 2B-C**. Examination of a ~50 kb slice of the genome reveals dozens of small occupancy peaks, with a visually apparent enrichment in intergenic regions (**Fig. 2B**). Many such peaks, which presumably correspond to individual protein binding events, coincide with known TF binding sites (TFBSs). For example, the region upstream of *argA* (**Fig. 2C**) shows strong occupancy at known ArgR binding sites, and condition-appropriate occupancy dynamics including weakening of binding in arginine-poor conditions [14,15] and loss of occupancy upon deletion of the *argR* gene. At the same time, similar occupancy patterns can be observed at many sites lacking an annotated TFBS, as seen in **Fig. 2D**, where a conditionally dynamic binding site is apparent between *lysA* and *lysR*, and a constitutive binding site in the *lysA* gene body. This dynamic site between the genes likely corresponds to binding of LysR itself in our minimal media condition, as LysR is known to bind somewhere in the region just upstream of *lysR* to repress transcription of *lysR* and activate transcription of *lysA* [16], but the precise location of the binding site has not previously been determined to our knowledge, and thus its exact coordinates are not present in common databases such as RegulonDB [7]. To facilitate inspection of other regions of interest, we provide complete occupancy traces for the conditions studied in **Supplementary Data S1**. As expected, at a genome-wide scale IPOD-HR signals show both significantly higher occupancy in intergenic regions relative to coding regions, and significantly higher occupancy at annotated TFBSs relative to other regions of the chromosome (**Fig. 2E**; see also **Table S1**), demonstrating a strong overlap of the observed protein occupancy with transcriptional

210 regulatory sites. Indeed, applying peak calling to the IPOD-HR signal demonstrates an increasingly strong overlap with known TFBSs as the threshold for peak calling is increased (**Fig. S1**).

215 It is also apparent by inspection of the genome-wide occupancy shown in **Fig. 2A** that many extended regions of high protein occupancy coincide with regions of relatively low transcription. For example, in **Figure 2F**, we show a typical ~300 kb region with alternating segments of high protein occupancy that have relatively low transcription, with those of low protein occupancy and relatively high transcription (also apparent in the higher-resolution plot in **Fig. 2G**). Thus, in addition to revealing occupancy at the level of individual regulatory sites, IPOD-HR enables tracking of the behavior of large, densely protein occupied regions of the chromosome that appear to coincide with transcriptionally silent loci. We will explore both of these prototypic classes of occupancy, in more detail, below.

### Transcription factor and sigma factor occupancy dynamics across genetic and environmental perturbations

225 Since IPOD-HR occupancy profiles show highly enriched overlaps with known TFBSs (**Fig. 2E**), we asked whether IPOD-HR profiles can be used to reveal the occupancy dynamics for known *E. coli* TFs across a set of conditions. Indeed, we find that IPOD-HR reveals consistent and condition-appropriate regulatory logic at the level of individual regulons, and patterns of regulatory behavior across regulons. As expected, strains with each of three single TF deletions (230 (*argR*, *lexA*, *purR*) show global loss of occupancy at the ensemble of annotated sites for the corresponding TFs (**Fig. 3A**) relative to growth under equivalent conditions of wild type cells (WT, rich). Analysis of condition-dependent changes in the occupancy of binding sites for single transcription factors likewise recapitulates expected behavior; for example, ArgR [17] and PurR [12,18] show enhanced binding to DNA in the presence of amino acid or nucleobase ligands (235 which are supplied directly in our rich media conditions, and the IPOD-HR occupancy signal shows global loss of occupancy for binding sites of both of these TFs in nutrient depleted conditions (minimal media and stationary phase) when compared with exponential growth in rich media (**Fig. 3A**). In contrast, RutR shows increased overall occupancy in minimal media relative to rich media conditions, consistent with the known inhibition of RutR binding by thymine and uracil [19]; similar behavior is observed for the cytidine-responsive CytR [20,21]. Sites for ArcA, (240 which becomes active under low oxygen conditions [22,23], show strong increases in occupancy in stationary phase at high culture density (**Fig. 3A**). Taken together, these findings demonstrate that IPOD-HR provides a quantitative readout of changes in regulatory activity across a broad range of physiological and genetic perturbations.

245 The utility of IPOD-HR in tracking the occupancy of known binding sites extends to global regulators with large characterized regulons; for example, comparison of the occupancy at annotated Lrp binding sites observed in IPOD-HR data to the occupancy of Lrp itself at the same sites in Lrp ChIP-seq data under similar conditions shows a significantly more similar (250 occupancy profile than is seen for other TFs with large regulons (**Fig. 3B**), as would be expected if the IPOD-HR profile were tracking Lrp occupancy across conditions. Importantly,

this concordance is maintained even in the presence of many other occupancy changes being measured for other proteins at locations throughout the genome, and potential interference from other factors binding to sites overlapping the Lrp sites.

255

Similar insights can be obtained across the *E. coli* transcriptional regulatory network by extending our analysis to all characterized TFBSs annotated in RegulonDB [7]; we show the resulting condition-dependent occupancies in **Fig. S2A**. As is apparent from the raw occupancies, *E. coli* transcription factors differ substantially from each other in the strength of the IPOD-HR footprint that they generate (leading, for example, to the very strong signals for factors such as IdnR). Across the conditions in our study, 122 out of the 176 TFs in RegulonDB had at least one site with detectable occupancy (robust z-score >3), and thus we are able to provide data on the characterized binding sites for the majority of TFs in *E. coli*. The remaining TFs likely represent a combination of factors that are not expressed or active under the limited set of conditions that we considered, and those that cannot be crosslinked efficiently to DNA by formaldehyde (e.g., Lac repressor, which was previously shown not to crosslink effectively to DNA with formaldehyde [24], and does not show substantial IPOD-HR signal) or do not partition appropriately in the phenol-chloroform extraction. For the majority of factors showing detectable occupancy, condition-dependent dynamics can be observed most clearly by normalizing the TF-level occupancy by the highest occupancy condition observed for that factor (**Fig. S2B**).

260

265

270

By applying an unsupervised clustering approach (see Methods for details), we identified transcriptional regulatory modules that show consistent co-regulation across the conditions in our study. We found clustering of TFs with highly similar behavior (**Fig. 3C**) that coordinate, for example, oxidative metabolism (red), amino acid uptake and synthesis (brown), and iron homeostasis (green). We also observe several cases where related regulators or regulatory cascades are clustered together; for example, the well-known regulators of carbon metabolism Cra and CRP (blue), NtrC and its transcriptional activator Fis (purple), or the tightly intertwined acid response regulators GadE, GadW, and GadX (pink). In order to test whether the co-clustering more generally indicated a significant overlap in the regulons of factors, or merely that they respond similarly to changing conditions, we calculated the pairwise Jaccard indices (that is, the size of the intersection of regulons between two TFs divided by the size of their unions, in terms of number of regulated genes) for all pairs of TFs considered in our analysis. We then compared the distribution of Jaccard indices for TFs which came from the same cluster, to that of Jaccard indices for pairs of TFs that did not co-cluster in **Fig 3C**. TF pairs that co-clustered were almost equally likely to have a non-zero Jaccard index (and thus share at least some regulatory targets) than were TF pairs from different clusters (odds ratio 0.95, p=0.76, Fisher's exact test). Thus, co-clustering appears to reflect different transcription factors that have similar condition-dependent occupancy profiles, rather than factors that regulate identical targets (likely minimizing redundancy of regulatory information in favor of combinatorial regulation of a single target by factors that each sense different stimuli). We expect that substantially more insight into these patterns may be obtained in the future through application of IPOD-HR to a broader array of conditions.

275

280

285

290

295 We thus find that IPOD-HR occupancy profiles can provide detailed, site-level, condition-specific  
information on regulatory protein occupancy across the entire chromosome. By comparing  
changes in protein occupancy with changes in transcript levels across conditions, we can relate  
changes in protein occupancy to their positive or negative regulatory consequences. This can  
300 be seen for two nutrient sensing transcriptional repressors with sites annotated in RegulonDB,  
ArgR and PurR, across changes in nutrient conditions (**Fig. 3D**). The changes in protein  
occupancy and regulatory output at these sites show that for both factors, there is a strong loss  
of protein occupancy at repressive ArgR and PurR sites, and a corresponding increase in  
transcriptional output in regulated genes, when considering minimal media relative to rich  
media.

305

Since each IPOD-HR global protein occupancy data set is performed alongside an RNA  
polymerase ChIP-seq experiment, we can easily track promoter occupancy alongside TFBS  
occupancy. The use of rifampin permits transcriptional initiation, but prevents elongation past a  
310 few nucleotides [25]. Thus, these data sets are ideal for identifying regulation at the level of  
RNA polymerase (e.g. via different sigma factors). The differential patterns of RNA polymerase  
occupancy show strong correlations with transcript levels for each Sigma factor's regulon across  
a range of conditions. As shown in **Figure 3E**, when comparing logarithmic vs. stationary phase  
conditions, the changes in transcript abundance and RNA polymerase promoter occupancy  
315 show a Spearman correlation of 0.94 ( $p=0.005$ ); an equivalent comparison for changes in  
occupancy vs. expression for cells grown in minimal media yields similar results (Spearman  
correlation 0.77,  $p=0.072$ ).

In addition to revealing the occupancy of individual, well-separated TFBSs, IPOD-HR  
320 occupancy can also yield insight into TF behavior at regulatory regions bound by multiple  
factors. An example is shown in **Figure 3F** for the *potF* promoter, which contains closely spaced  
Lrp, ArcA, and ArgR binding sites. The observed occupancy profile appears decomposable into  
a contribution from Lrp binding (strong in minimal media, and moderate in the RDM conditions),  
ArgR binding (strongest in rich media, moderate in stationary phase RDM and in minimal media,  
325 and absent in  $\Delta argR$  cells), and ArcA binding (mainly in stationary phase). Binding of the Lrp  
site at the *potF* promoter is known to be strongest in minimal media, and weaker but still present  
in RDM (both in exponential and stationary phase; see Fig. 4A of [26]); the broad occupancy  
around the annotated Lrp site is likely due to weaker binding of other sites from the Lrp octamer.  
The inferred behaviors of ArgR and ArcA binding are likewise consistent with the overall  
330 behavior of sites for those TFs in our experiments (**Fig. 3A** and **S2**). A more complex example  
can be seen in **Fig. 3G**, where we show the *ndh* promoter containing overlapping binding sites  
for six different transcription factors. At such a complex promoter, deconvolution of the observed  
occupancy is still possible subject to consistency assumptions (that sites for a given TF will all  
change occupancy in the same direction in unison, even if by different amounts). Based on this  
335 assumption, the predominant contributors to binding at the *ndh* promoter appear likely to be IHF  
and PdhR in the "WT,rich" condition, IHF and NsrR in the "WT,minimal" condition, and NsrR and  
ArcA in the "WT,stationary" condition. However, assignments of occupancy to specific factors at  
such a complex promoter cannot be made with certainty on the basis of IPOD-HR data alone;



340 combination with ChIP data under similar conditions (as invoked in the discussion above for **Fig. 3F**) can aid in assignment, as could more formal methods for deconvolving the protein occupancy signal based on the overall distribution of sites for each factor across the genome (similar to the approach taken by CENTIPEDE for eukaryotic chromatin accessibility data [27]); development of such analysis tools is an area of active research.

### 345 **Global occupancy dynamics reveals the action of new DNA binding proteins**

Despite extensive annotation efforts, at present fewer than 1,100 of the 3,560 annotated transcriptional units present in the RegulonDB database have any annotated regulation by transcription factors assigned to them [7]. While several recent notable efforts have sought to expand the completeness of these regulatory annotations by studying the DNA binding preferences of purified TFs [6,28,29], or via computational inference of likely additional regulation [30] and regulatory modules [31], none of these methods provides either direct evidence for binding *in vivo*, or information on condition-dependent changes in occupancy. IPOD-HR, in contrast, can provide both. Furthermore, the protein occupancy signals thus obtained provide information on occupancy of both well-characterized and uncharacterized proteins. In fact, many dynamic IPOD-HR peaks occur in promoters with no previous annotation for TF binding sites, as we will discuss in detail in the following section.

A representative example of an orphan occupancy peak is seen upstream of the gene *sdaC* (**Fig. 4**). In our RNA-seq data, *sdaC* transcript levels are nearly twenty-fold higher during exponential growth in rich media (317.3 transcripts per million (TPM)) compared with either exponential growth in minimal media (17.9 TPM) or stationary phase in rich media (16.7 TPM). Despite a lack of annotated TFBSs upstream of *sdaC*, IPOD-HR occupancy profiles (**Fig. 4A**) show a likely transcriptional activator binding site upstream of the *sdaC* core promoter, which shows strong occupancy in the WT M9/RDM/glu conditions but not the related conditions where *sdaC* expression is lower. To identify the transcription factor(s) responsible for that occupancy, we used a biotinylated bait DNA matching the sequence of the *sdaC* promoter region to isolate proteins bound to that region from *E. coli* cells grown in the WT M9/RDM/glu condition (**Fig. 4B**). Mass spectrometry on isolated bait-dependent bands revealed two poorly characterized transcription factors, UlaR and YieP, that showed highly enriched binding to the *sdaC* promoter (see **Supplementary Table S2**). While UlaR proved difficult to purify due to poor solubility, and was thus excluded from further analysis, we found that purified YieP does indeed show specific shifting of the *sdaC* promoter in an electrophoretic mobility shift assay (**Fig. 4C**). Consistently, recent RNA-seq data on a  $\Delta yieP$  strain shows a significant drop in *sdaC* transcript levels (2.7-fold change;  $q=7.6 \times 10^{-18}$ ) relative to isogenic cells with a plasmid-born reintroduction of YieP during growth in LB media (C. Bianco and C. Vanderpool, personal communication).

YieP was recently (and independently) selected by Palsson and co-workers as a validation case to be used in their consideration of computational methods for identifying the binding sites of orphan TFs, and subjected to ChIP-exo analysis on cells grown in glucose minimal media using epitope-tagged YieP [30]. Indeed, their data demonstrate both strong direct YieP occupancy, and a high confidence YieP motif match, at the precise position of the occupancy peak detected

in our IPOD-HR data set (**Fig. 4D**). Based on the relative intensity at that position across conditions, combined with the expression data noted above, we infer that YieP binds to the *sdaC* promoter in nutrient-replete conditions and acts as a transcriptional activator (explaining the solitary strong peak in our “WT,rich” condition), whereas in other conditions, YieP binding is weakened (but not abolished) and additional factors likely bind downstream of the YieP site to repress *sdaC* transcription.

We must emphasize that the discovery of YieP binding sites through IPOD-HR and subsequent mass spectrometry experiments (by us) occurred in parallel with the ChIP-exo experiments of Gao and colleagues, and indeed, represent highly complementary paths for identification of the binding sites for orphan transcription factors, with one centered on a candidate protein and the other on candidate sites.

In order to directly assess the regulatory role of the identified YieP binding sites, we integrated a *lacZ* reporter at the *araBAD-araC* locus in both WT and  $\Delta yieP$  backgrounds, driven by variants of the *sdaC* promoter that either match the original sequence, or have one or both YieP binding sites scrambled (see Methods for details). Consistent with the RNA-seq data described above, we observed that deletion of *yieP* leads to a significant drop in reporter activity with the wild type *sdaC* promoter (**Fig. 4E**, “WT *sdaCp*”). Interpretation of the single-site scrambles is complicated by the fact that the promoter variants appear to have substantively different effects in the WT and *yieP* backgrounds; however, what is clear is that removal of both YieP binding sites (**Fig. 4E**, “Site 1/2 scramble”) leads to a drop in reporter activity in the WT background that is virtually identical to that observed with deletion of *yieP*, whereas in a *yieP* background there is instead a significant increase in reporter activity when the sites are scrambled. The sign epistasis observed between *yieP* genotype and the presence of YieP sites at the *sdaC* promoter argues that the observed YieP binding sites are functional regulatory sites, but that YieP also acts indirectly at this promoter (either through alterations of cellular physiology in the *yieP* background or genetic interaction with another regulator acting at this promoter, eg. by repressing and/or directly competing for binding with a repressor that acts here). The example presented here of regulation of *sdaC* by the uncharacterized transcription factor YieP highlights the broad potential for using IPOD-HR to rapidly identify and characterize previously cryptic regulatory connections. IPOD-HR thus complements the multitude of other approaches noted above (based on, e.g., promoter libraries or computational inference), and provides the unique benefit of directly assessing binding to DNA *in vivo*, at native loci, under physiological conditions of interest.

The utility of IPOD-HR in identifying the activity of previously un-characterized transcription factors motivates its extension to a genome-wide scale, providing an *in vivo* complement to high-throughput *in vitro* screening methods such as genomic SELEX [6]. By applying peak calling to our IPOD-HR data sets across the six conditions considered in the present study, we were able to identify thousands of likely TFBSs, many of which are not identifiable based on existing databases. A comprehensive listing of peak calls across conditions and thresholds is given in **Supplementary Data S2**. To compare the peak sets identified from IPOD-HR data with our existing state of knowledge, we divided the peak calls obtained from IPOD-HR into a set of

430 annotated TFBSs from RegulonDB, and a set of binding sites predicted using all known PWMs available in the SwissRegulon database (see Methods for details). We find that across a range of thresholds, approximately half of the binding sites identified by IPOD-HR overlap with either known or predicted sites, whereas the other half represent novel binding sites which likely (as in the case of the YieP site described above) reflect the activity of poorly annotated or orphan TFs. Pooling the newly identified binding sites across conditions, our IPOD-HR data sets are able to provide a total of 14,271 putative TFBSs, representing 5,090 unique sites, which are occupied *in vivo* under at least one condition; we also track the dynamics of occupancy of those sites across conditions. This extensive map of chromosomal occupancy and its dynamics  
435 provides the community with a wealth of known and putative novel regulatory interactions that can be further explored and validated by follow-up experiments such as those shown in **Fig. 4**. It is also possible to cross reference the newly identified binding sites with high throughput studies of potential binding locations for newly characterized TFs (e.g., ChIP or genomic SELEX [28] data) to identify potential factors binding to a region of interest, and to use the IPOD-HR  
440 occupancy maps to obtain initial estimates of the condition-dependent occupancy of any identified sites.

### Global *de novo* discovery of sequence-specificity motifs for active transcription factors

445 While the peak calls obtained from IPOD-HR data show strong enrichments with known TFBSs (**Fig. S1**), many of the called peaks do not match any known or predicted transcription factor binding sites (as detailed in **Figure 5A**), and likely correspond either to unknown sites for well-characterized TFs or binding sites for previously uncharacterized TFs. Given that the majority of the newly inferred binding sites appear not to correspond to known or predicted sites for annotated TFs, we hypothesized that the regulons corresponding to those motifs would likely  
450 show enrichments for poorly annotated genes, as we expect here to reveal the regulatory logic driving typically under-studied pathways. We thus identified likely regulatory targets of each newly called peak, divided them between poorly annotated genes (those with UniProt annotation scores of 1 or 2 out of 5 [32]) and well-annotated genes, and then examined the proportion of poorly annotated targets for occupancy peaks matching RegulonDB binding sites  
455 compared with all other peaks. As shown in **Figure 5B**, peaks that do not correspond to RegulonDB-annotated binding sites are strongly enriched upstream of poorly annotated genes, whereas those matching annotated binding sites are enriched for well-annotated genes. Thus, examination of occupancy peaks derived from IPOD-HR enables identification of a large number of new putative regulatory sites, with a particular abundance of possible regulators of  
460 poorly-annotated genes.

Our large-scale identification of new TFBSs also raises the important possibility that new TF binding motifs might likewise be identifiable through *de novo* computational motif discovery in the set of all sequences within IPOD-HR peaks. Indeed, the application of the FIRE [33] motif  
465 discovery algorithm to peak locations obtained from IPOD-HR data reveals hundreds of *de novo* discovered sequence motifs that are informative of strong occupancy sites, even after pruning of redundant motifs (**Fig. 5C**). Upon cross-referencing with a database of known *E. coli* TFBS

motifs using TOMTOM [34], we find that approximately 25% of the discovered motifs can be  
470 matched with known motifs (notably, 86/97 of the annotated motifs in the *E. coli* SwissRegulon  
database are matched by at least one inferred motif from the set present prior to redundancy  
pruning, and 68/97 match at least one motif present in our inferred set after pruning), while at  
the same time nearly 200 novel motifs are called with similar confidence (**Fig. 5D**). A  
comprehensive list of redundancy-pruned motifs called across all conditions in our study is  
475 given in **Supplementary Data S3**. To provide estimates of the false discovery rate (FDR)  
arising from our motif inference, we performed an identical motif discovery procedure for each  
biological condition on 20 “decoy” data sets in which the underlying *E. coli* genomic sequence  
was rotated by a random distance relative to the peak calls, thus preserving the correlation  
structure of both the data and sequence with respect to themselves (light bars in **Figure 5C**).  
Our decoy data sets gave rise to no more than 1 motif under any condition, giving rise to an  
480 effective FDR (across shuffles and conditions) of less than 0.5% even for our fully pruned  
motifs. Using only the novel motifs (that is, motifs which did not have detectable similarity to any  
motifs in the SwissRegulon database) in a genome-wide search for potential binding sites using  
FIMO, we find that 84.8% of all IPOD occupancy peaks at a peak calling threshold of 4 can be  
485 explained by binding sites for the novel motifs, compared with 7.5% that can be explained by  
annotated binding sites from RegulonDB (predicted binding sites for all newly inferred motifs  
from the IPOD-HR data are enumerated in **Supplementary Data S4**). Thus, the newly inferred  
motifs provide a substantially expanded ability to assign the observed profile of protein binding  
across the chromosome.

490 In **Figure 5E** we show two representative examples of discovered motifs that show strong  
matches with annotated motifs, demonstrating that the motifs for well-characterized  
transcriptional regulators such as CRP and NanR can be inferred directly from IPOD-HR data.  
For comparison, in **Figure 5F**, we show two newly inferred motifs that do not match any known  
motifs in the *E. coli* SwissRegulon database. Intriguingly, the pattern of binding sites across the  
495 *E. coli* chromosome for both of these novel motifs illustrates a potential regulatory function, with  
the first motif associating with a substantial fraction of the genes involved in import and  
metabolism of low preference carbohydrates, and the second apparently involved in iron  
acquisition and regulation of protein catabolism. In order to provide additional insight into the  
potential physiological roles of the factors binding these motifs, we considered the similarity of  
500 their putative regulons to those of well-characterized transcription factors, making use of the  
Jaccard index comparing the gene sets potentially regulated by each motif with those of known  
TFs. For the top motif shown in **Fig. 5F**, the best match is for CRP, with a Jaccard index of 0.19.  
This finding is consistent with the putative role in regulating carbon source utilization, although  
the regulon of the new motif is clearly distinct from those of any well-characterized factor given  
505 that the highest Jaccard index observed for it was 0.19, and the next highest hit after CRP was  
0.12. Applying the same analysis to the bottom motif shown in **Figure 5F** shows that the  
strongest detectable similarity in regulons is to those of H-NS (0.12) and Fur (0.11). These  
matches indicate potential roles for the new motif in coordinating responses to changes in iron  
starvation and other stress conditions such as changing temperatures, but again, the regulon of  
510 the newly identified motif is clearly quite distinct from that of the characterized TF. In order to  
facilitate similar analysis of the potential functions of the other newly inferred motifs, we provide

in **Supplementary Data S8** the Jaccard indices for all significant overlaps between the putative regulons of our newly inferred motifs, and those of existing factors as annotated in RegulonDB (see caption for details).

515

We further assessed the regulatory capacity of all newly called sequence motifs by comparing their genome-wide distribution of binding sites with annotated genes (coding regions) and promoters. We would expect that binding sites for functional transcriptional regulators would be enriched within promoters and depleted from coding regions, as was the case for overall IPOD-HR occupancy (**Fig. 2E**). Indeed, the overlap distributions of binding sites for our newly inferred motifs are uniformly enriched for annotated promoters and depleted for ORFs (**Fig. 5G**;  $p=1.0 \times 10^{-27}$ , Wilcoxon rank sum test), demonstrating that motifs inferred directly from IPOD-HR occupancy data occur primarily in likely regulatory regions. Equivalent results were obtained even after excluding all of the newly inferred motifs with identifiable similarity to SwissRegulon motifs (as assessed using TOMTOM; data not shown). To further investigate the global regulatory potential of the newly inferred motifs, we applied iPAGE [35] to identify cases of significant mutual information between predicted binding sites for a given motif (within 100 bp of an annotated transcription start site in RegulonDB), and the corresponding Gene Ontology terms of genes in the potentially regulated operons. We found that out of a total of 1,638 motifs with identifiable binding sites, 1,518 have significant mutual information with genes from at least one GO term (notably including 114 out of the 123 non-redundant motifs that had identifiable binding sites by our criteria, and no detectable similarity to previously known motifs). These findings highlight potential pathways that may be regulatory targets of these newly inferred motifs; the resulting predicted regulatory targets are summarized in **Supplementary Data S5**. In the future, tracking of the occupancy of these motifs over a broader range of physiological conditions would yield additional insight into the likely stimuli sensed by them, and the downstream processes that they may regulate.

520  
525  
530  
535

Given that the majority of the newly inferred motifs appear not to correspond to annotated TFs, and our findings above regarding the enrichment of poorly annotated genes downstream of orphan binding peaks, we hypothesized that the regulons corresponding to our newly inferred motifs would likely show enrichments for poorly annotated genes, as we expect here to reveal the regulatory logic driving typically under-studied pathways. We thus calculated the fractions of the hypothetical regulons of each newly inferred motif that consist of poorly annotated genes (defined as noted above). As shown in **Figure 5H**, we found that the regulons of the newly inferred motifs were significantly enriched for poorly annotated genes when compared with both the annotated *E. coli* transcriptional regulatory network in RegulonDB ( $p=5.92 \times 10^{-10}$ , Wilcoxon signed rank test), and the overall average rate of poorly annotated genes throughout the chromosome ( $p=2.10 \times 10^{-5}$ , Wilcoxon signed rank test). Pairwise comparison of the rate of poorly annotated genes between the regulon of each newly inferred motif and all genes that were not members of the corresponding regulon likewise showed a significant enrichment for poorly annotated genes ( $p=2.10 \times 10^{-5}$ , Wilcoxon signed rank test). Taken together, we see that IPOD-HR enables inference of a large number of sequence motifs, many of which likely correspond to functional, but currently under-studied, transcriptional regulators in *E. coli*, providing a substantial resource for ongoing investigation of this transcriptional regulatory network.

540

545

550

555

## Extended protein occupancy domains define distinct and largely stable transcriptionally silent regions with unique sequence features

One of the most striking findings enabled by the original application of IPOD was the discovery of extended protein occupancy domains (EPODs): large regions of the *E. coli* chromosome that show unusually dense levels of protein occupancy over kilobase or longer scales [10]. EPODs are also clearly apparent in all our IPOD-HR data sets, and appear to correspond functionally to the transcriptionally silent tsEPODs of Vora *et al.* [10]. The profile of protein occupancy and EPODs, along with the accompanying impacts on transcript levels, for a representative region of the genome is shown in **Figure 6A**. Indeed, we found that many highly protein occupied regions measured using the original IPOD method (in particular, the highly expressed extended protein occupancy domains, or heEPODs) represent RNA polymerase occupancy, whereas the EPODs now revealed by IPOD-HR consist solely of large domains of occupancy by proteins other than RNA polymerase (which typically also exclude RNA polymerase). We discuss these differences and the details of the approach used in IPOD-HR to remove contributions from RNA polymerase in **Text S1**. The specific resolution of tsEPODs afforded by the IPOD-HR method, and the coverage of multiple genetic and nutrient perturbations in the present data sets, allow us to fully investigate the nature and condition-dependent occupancy of these chromosomal structures.

The identified EPODs show remarkable stability (**Fig. 6B**), with ~200 EPODs in each physiological condition (or ~450 using a relaxed calling threshold; see Methods for details), and similar fractions of the genome contained in EPODs in each case. A comprehensive listing of EPODs identified across our conditions is given in **Supplementary Data S6**. The  $\Delta argR$  strain serves as an outlier amongst the genetic perturbations, with modestly decreased (but still substantial) EPOD coverage, possibly due to decreased expression of H-NS in this condition (RNA polymerase occupancy of the *hns* promoter measured in our ChIP dataset is two-fold lower than in WT cells under equivalent conditions; it is unclear whether this reflects a regulatory or metabolic effect caused by loss of ArgR). The differing behavior of the  $\Delta argR$  strain appears milder using the relaxed EPOD calling threshold, and thus the difference is at least partially just a thresholding effect (**Fig. 6B**). The locations of individual EPODs are likewise well maintained, even across very different physiological conditions. For example, in **Figure 6C** we show IPOD-HR occupancy across the same region as shown in **Figure 6A**, comparing exponential growth in rich vs. minimal media, and stationary phase cells. In contrast with the condition-dependent occupancy of individual TFs, at the ~kilobase scale the occupancy traces are nearly superimposable, and show that most EPODs called under the various conditions overlap. Furthermore, out of the subset of EPOD calls that are present in the 'WT,Rich' condition but absent in the others, all are present in the 'WT,minimal' condition using the relaxed EPOD calling threshold, and all but two also present in the stationary phase condition using that threshold, suggesting that many of the small differences in EPOD locations that do appear between EPOD calls under different physiological conditions are in fact due to thresholding effects. We observe the same trends genome-wide: aside from the  $\Delta argR$  case, 71-86% of genomic locations (at the base pair level) that are called as EPODs under any one condition are likewise EPOD calls under any other condition (**Fig. 6D**); furthermore, at least 86% (and typically much more) of the EPODs called in one condition are contained within the relaxed threshold calls under any other condition (*n.b.* the 'relaxed' threshold used here corresponds

600 with the original EPOD definition from [10]). It is also worth noting, in this context, that 89% of the tsEPOD-occupied locations from [10] are contained in the new “WT,Rich” relaxed threshold EPOD set, in line with the observed concordance across experimental conditions in our new data sets.

605 Several defining characteristics of EPODs are readily apparent upon cross-referencing with other genome-wide datasets (**Fig. 6E**): they represent regions of high AT content, which are both associated with low levels of native transcripts and decreased transcriptional propensity (that is, expression of standardized integrated reporters [36]). Consistent with our original findings [10], EPODs also show high occupancy of H-NS, HU, and LRP; low occupancy of Fis; and are associated with high efficiency of Tn5 integration (**Fig. 6E**). While the latter might seem  
610 surprising given that highly protein occupied regions on eukaryotic chromatin tend to exclude Tn5 (as is used to great effect in ATAC-seq [37]), we note that bacterial H-NS occupancy has previously been shown to facilitate Tn5 activity [38]. Additional characteristics of EPODs, such as reduced densities of possible Dam methylation sites (consistent with the expected blocking  
615 of Dam methylase by bound proteins, previously shown in *in vivo* methylase protection experiments [39]) and a characteristic pattern of DNA structural parameters including decreased minor groove width, are shown in **Table S3**.

The remarkable condition-invariance of the locations of EPODs outlined above, even across  
620 such dramatic changes as transition from exponential to stationary phase, suggests that EPODs predominantly represent fixed structural features of the *E. coli* chromosome, rather than highly dynamic regulatory structures. We thus examined the classes of genes (assessed using gene ontology, or GO, terms) most strongly enriched or depleted in EPODs. As illustrated in **Figure 7A**, EPODs show strong enrichments for mobile elements (GO:0006313) and prophage genes (specifically lytic pathways; GO:0019835), and are depleted for core metabolic pathways such  
625 as ribosome components (GO:0005840). Indeed, EPODs are associated with the silencing of many prophages (e.g., **Fig. 7B**) and even smaller operons of unknown function (e.g., **Fig. 7C**).

Our findings regarding EPODs, particularly the high levels of H-NS binding in EPODs, and the  
630 known role of H-NS as a xenogeneic silencer [40,41], are highly consistent with prior information regarding the silencing role of H-NS. In order to determine the extent to which H-NS silenced regions and EPODs as defined here overlap, we compared the distribution of EPODs across the genome with H-NS ChIP-seq data from [42]. Using an unsupervised clustering method to divide genomic intervals into high, medium, and low levels of H-NS occupancy. We found that 72.4%  
635 of EPODs fall into the high H-NS category, compared with 5.4% of non-EPOD regions (**Fig. S3A**). Nevertheless, when considering the average transcript levels observed as arising from the same genomic intervals, the EPODs from the low H-NS and medium H-NS categories still showed significantly lower expression than non-EPOD regions with similar H-NS levels (**Fig. S3B**), and the small number of highly H-NS bound regions which are not part of EPODs are in  
640 fact more silent than highly H-NS bound EPODs. Taken together, we thus observe that while many EPODs represent chromosomal regions silenced by H-NS, roughly one-third to one-fourth of EPODs do not show the characteristics of highly H-NS occupied regions, but are nevertheless transcriptionally silenced by an extended stretch of high protein occupancy. The

645 possibility of course exists that H-NS is repositioned in the conditions of our study, which differ  
646 from those of [42], to cover the remainder of the EPODs identified here; however, we have  
647 shown in practice that this is not the case, as the non H-NS EPODs identified here persist even  
648 in a *hns/stpA* strain (Amemiya *et al.*, submitted). The mechanism of silencing at these non-H-NS  
649 dependent EPODs will likely be a fruitful area for future investigation.

## Discussion

650 The study of bacterial transcriptional regulatory networks has long benefitted from bottom-up  
651 approaches such as DNase footprinting, ChIP-chip, and ChIP-seq to map the behavior of  
652 individual factors and regulons. At the same time, however, the insight provided by such  
653 approaches has been inherently limited by the need to specify *a priori* the target of investigation,  
654 either in terms of the regulator, regulated gene, or both. However, as we hope to have  
655 demonstrated here, a global agnostic strategy (as exemplified by IPOD-HR) provides a unique  
656 top-down complement to existing methods by permitting rapid profiling of the protein occupancy  
657 landscape of a bacterial chromosome. We have demonstrated that IPOD-HR simultaneously  
658 enables resolution of individual changes in transcription factor binding at specific sites, inference  
659 of new regulatory motifs which likely correspond to functional but poorly characterized  
660 transcriptional regulators, and large-scale patterns of protein occupancy indicative of  
661 constitutively silenced genomic regions. IPOD-HR thus falls into the same family as methods  
662 such as DNase I hypersensitivity [43], MNase-seq [44], and ATAC-seq [37], but was from its  
663 inception developed, tuned, and validated for the unique molecular and biophysical features of  
664 bacterial chromosomes (we note that applications of ATAC-like methods to bacteria have  
665 recently been reported in preprints [45,46] post-dating the preprint of the present manuscript  
666 [47]).

667 We expect that all three key capabilities of IPOD-HR highlighted above will prove to be of  
668 substantial utility in investigating all cultivable bacterial transcriptional regulatory networks, and  
669 could potentially even be applied to environmental samples to study occupancy landscapes in  
670 uncultivable bacteria. The ability to directly track the occupancy of TFBSs for a large set of  
671 transcriptional regulators in parallel provides the missing link that has previously stymied efforts  
672 to predict the transcriptional output of *E. coli* across conditions, as consideration of only the  
673 expression levels of TFs to predict the behavior of their regulons has yielded mixed results  
674 [8,48]. Furthermore, the ability to identify likely regulatory sites even in the absence of prior  
675 knowledge, as shown both for isolated promoters (**Fig. 4**) and inference of entire regulons (**Fig.**  
676 **5**), will substantially accelerate our ability to complete a wiring diagram for the *E. coli*  
677 transcriptional regulatory network and to rapidly approach the networks of other less well-  
678 characterized bacterial species. In the latter case, we expect that the ability of IPOD-HR to  
679 highlight the locations of transcription factor binding sites, and the demonstrated feasibility of  
680 inferring DNA-binding protein sequence motifs based on those sites, will allow the rapid  
681 identification of sites of interest for detailed follow-up studies (e.g., application of pulldowns  
682 similar to those in **Fig. 4** to identify the precise factor(s) occupying a particular motif). The  
683 resulting information will provide an essential set of building blocks to aid in the overall  
684 reconstruction of a transcriptional regulatory network. In addition, tracking of the occupancy of  
685



different motifs across conditions will likely assist in the identification of biological conditions pertinent to the function of the factor binding each motif, and cross-referencing with RNA polymerase occupancy will provide evidence on the sign of regulatory output associated with each site. IPOD-HR thus provides a powerful high-throughput *in vivo* approach tracking  
690 occupancy at native sites, complementing methods based on screening with purified proteins [28], computational inference [30], or reporter assays [29].

Our study of diverse experimental conditions across different genetic and physiological states provides a comprehensive view of the protein-DNA interactome of *E. coli*. As we have shown,  
695 the majority of discovered occupancy events do not correspond to previously known or annotated sites of protein-DNA interactions. We have further shown that these global occupancy profiles can be used for wholesale discovery of sequence specificity for the set of TFs active under these conditions. These occupancy maps and the corresponding DNA motifs provide the community with a rich catalogue of likely regulatory events to study, targeting either  
700 particular genes or larger pathways. Indeed, our finding that the novel occupancy sites and DNA motifs are highly enriched upstream of genes that are under-studied promises to discover and expand the physiological and regulatory modules of *E. coli*.

Our study also provides significant additional evidence for the presence of large,  
705 transcriptionally silent, high occupancy chromosomal domains in *E. coli*, termed EPODs. Many such EPODs clearly correspond to regions of H-NS binding, which has previously been shown to form several types of filaments that silence horizontally acquired DNA [5,41,49–51]. On the other hand, we also observe a substantial fraction of EPODs that do not correspond to H-NS binding, and yet are still associated with transcriptionally silent regions of the chromosome.  
710 Numerous questions regarding the nature and role of those EPODs remain for future work, including: what is the protein composition of non-H-NS EPODs? What rules dictate their formation on specific sites? We are also tempted to speculate that in some contexts non-H-NS EPODs may undergo condition-dependent changes in occupancy that drive transcriptional regulation, although no such cases could be definitively identified in the conditions studied here.  
715 Such behavior has already been observed for H-NS filaments in various enterobacteria [52,53]. Ongoing application of IPOD-HR to a broader range of physiological conditions in *E. coli* will provide further insight into the overall landscape of large-scale protein occupancy across conditions, allowing tracking both of occupancy associated with H-NS (and the related protein StpA) and other classes of EPODs in a single experiment.

720 Our IPOD-HR strategy for mapping the global dynamics of the *E. coli* protein-DNA interactome relies only on simple physico-chemical principles for isolating protein-DNA complexes. As such, it is easily transferable to other bacterial species. The rich and comprehensive data sets that would result, and application of statistical inference during data processing as exemplified here,  
725 will provide important regulatory roadmaps in organisms with less well studied transcriptional regulatory networks, such as non-model bacterial species of clinical and industrial importance. In the future, applications to a broader range of physiological conditions (in *E. coli*) and to other bacterial strains and species will provide important information on the role of large-scale

730 nucleoprotein assemblies on gene regulation, and pave the way for more comprehensive and  
predictive models of transcriptional regulatory logic.

735

## Figures

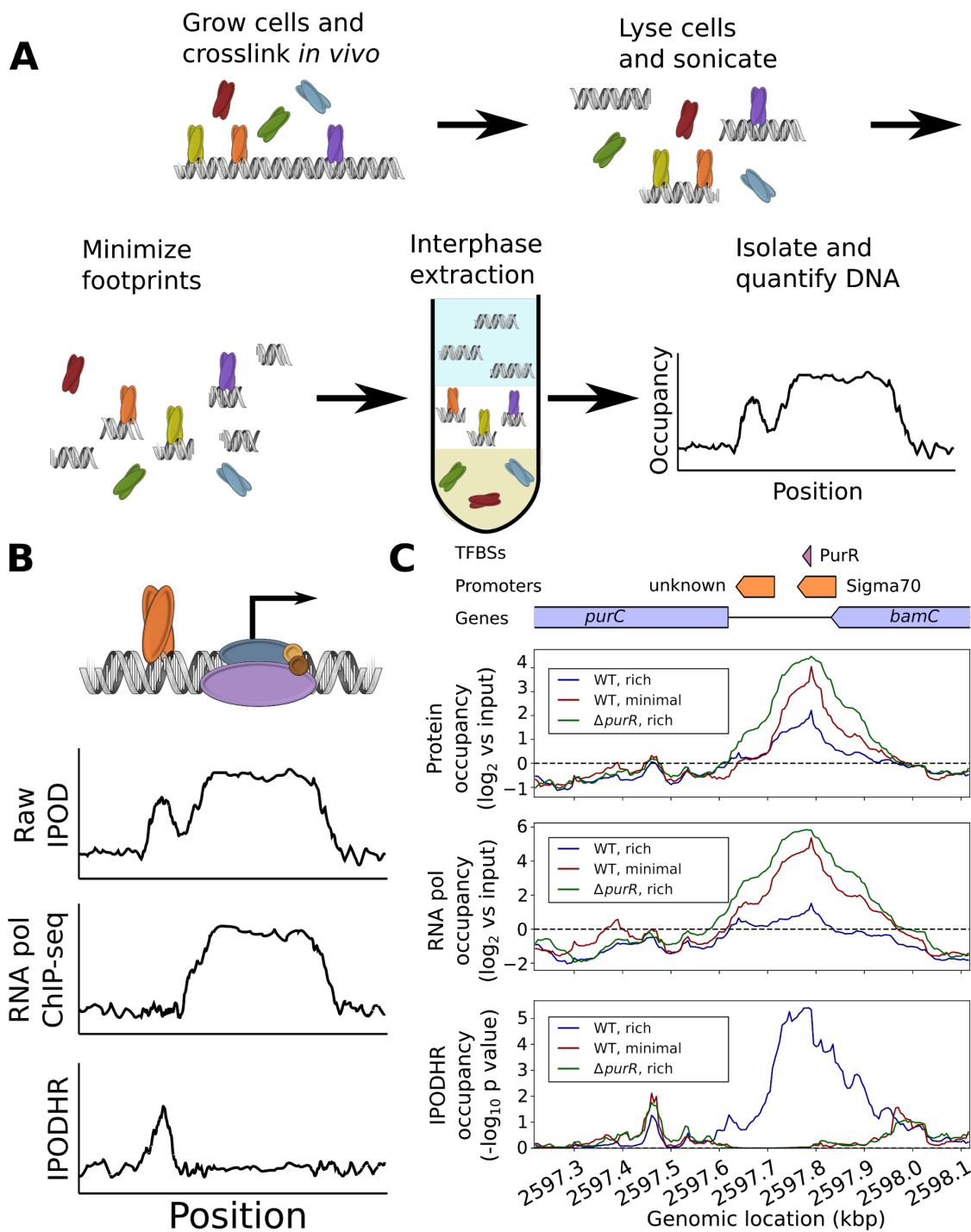


**Figure 1: Schematic of IPOD-HR technology and detection of context-dependent binding by transcription factor PurR. (A)** Overall workflow for isolation of the IPOD-HR fraction and quantification of total protein occupancy. **(B)** The final IPOD-HR signal is obtained by subtracting a normalized RNA polymerase occupancy signal from the raw IPOD-HR protein occupancy, resulting in a polymerase-corrected signal. **(C)** Example of RNA-polymerase corrected IPOD-HR profile upstream of the *purC* gene, where subtraction of RNA polymerase occupancy from the raw IPOD-HR signal properly reveals a PurR binding site in rich media that is lost upon deletion of *purR* or transition to minimal media. In the schematic above the plots, blue regions show genes, orange regions show promoters, and purple regions show annotated transcription factor binding sites.

750

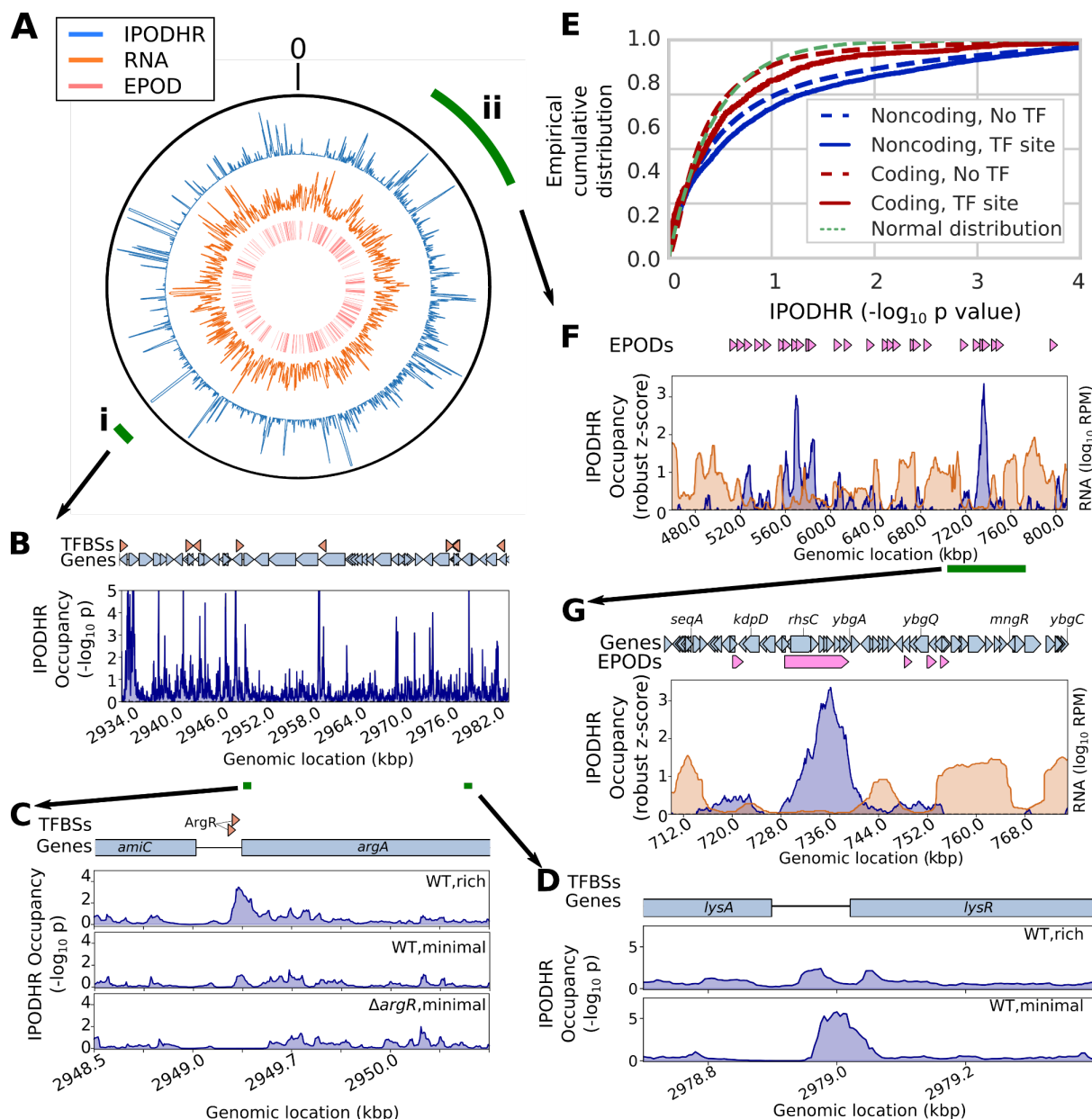


**Figure 2: IPOD-HR profiles reveal rich high-resolution occupancy dynamics and large-scale structural features across the chromosome.**

**(A)** *Outer track*: IPOD-HR occupancy (robust Z-scores, 5 kb moving average); *middle track*: total RNA read density (5 kb moving average); *inner track*: locations of inferred EPODs. The outer green wedges mark the portion of the chromosome shown in subsequent panels. The origin of the coordinate system is oriented at the top of the plot. All data in this figure are for the “WT,rich” condition unless otherwise noted.

**(B)** IPOD-HR occupancy measured during growth in glucose rich defined medium, in the vicinity of wedge i from panel A. Green segments below the genomic coordinates indicate the regions highlighted in panels C-D. **(C)** Condition-dependent occupancy changes at the ArgR binding sites upstream of *argA*. **(D)** Identification of condition-specific occupancy of a likely LysR binding site between *lysA* and *lysR*. **(E)** Cumulative histograms showing RNA polymerase ChIP-

755

760

765 subtracted IPOD-HR occupancy in coding vs. noncoding regions, and at sites that match known  
transcription factor binding sites from RegulonDB [7], compared with the curve that would be  
expected from a standard normal distribution of scores. Additional descriptive statistics and  
significance calls are given in **Table S1**. **(F)** Occupancy (blue) and total RNA abundance  
(orange) for a selected sector of the genome (wedge **ii** from panel **A**), showing the presence of  
several EPODs in regions corresponding to low RNA abundance; rolling medians over a 5 kb  
770 window are plotted, with RNA read densities shown in units of reads per million (RPM). **(G)**  
Magnification of the region highlighted by the green bar in panel **F**, illustrating a silenced region  
in and around *rhsC*, alongside flanking areas of low IPOD-HR occupancy and high transcription.  
A 5 kb rolling median is plotted.

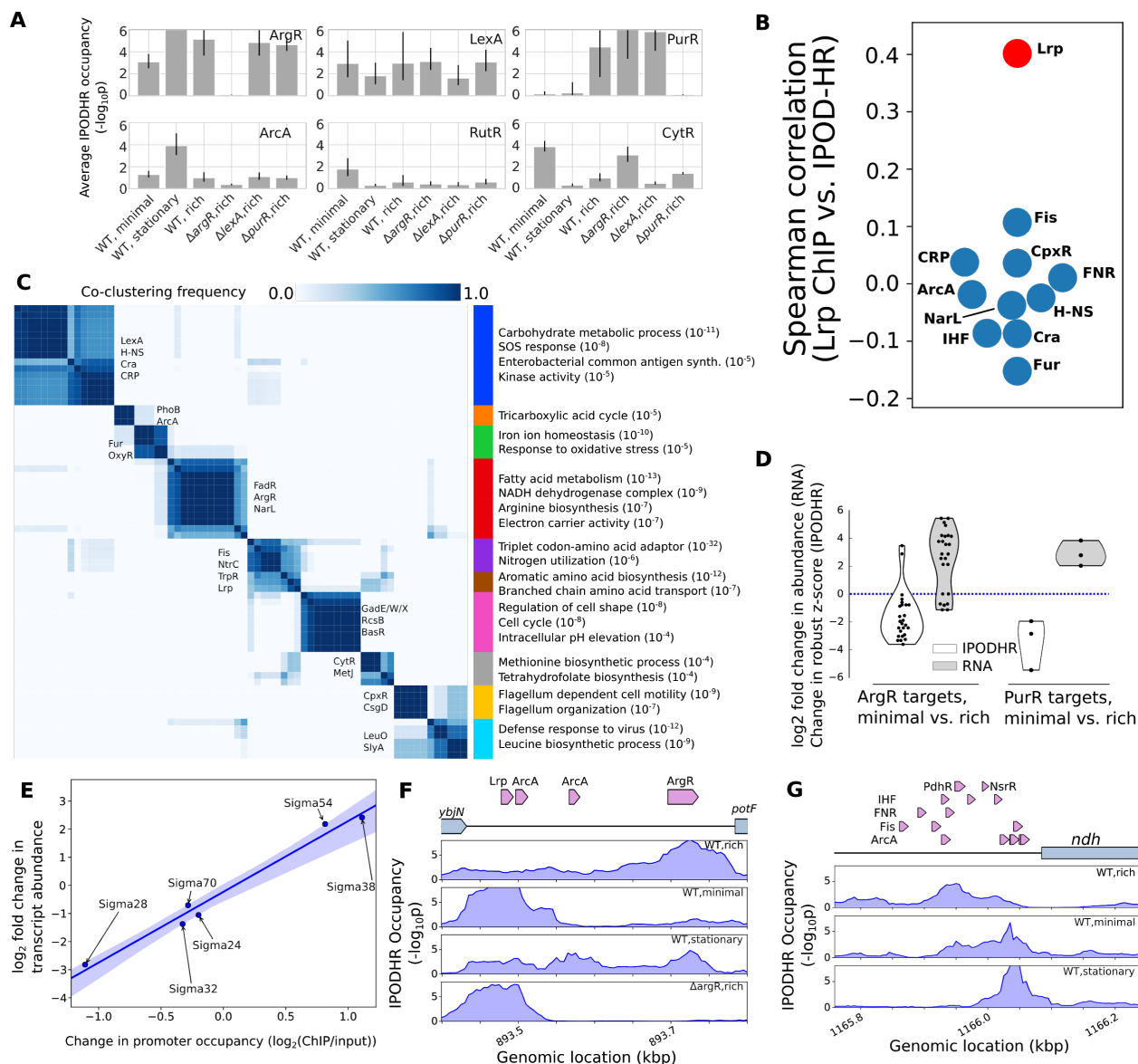


**Figure 3: IPOD-HR profiles reveal global binding activity of known transcription factors and sigma factors.** (A) Average (geometric mean) occupancies for all annotated binding sites of the six indicated transcription factors under each indicated condition. Error bars indicate a 95% confidence interval based on parametric bootstrapping with pessimistic assumptions; see

775 Methods for details. The number of detectable sites used to estimate the condition-specific occupancies were 30, 10, 2, 45, 6, and 9 for ArgR, LexA, PurR, ArcA, RutR, and CytR, respectively. (B) Spearman correlations between all occupancy values at annotated binding sites for the indicated transcription factors (all TFs with at least 50 sites in the RegulonDB database) in the IPOD-HR vs. Lrp ChIP data sets. Points shown in red have a statistically significant correlation (FDR-corrected p-value < 0.05). Annotated binding sites are from RegulonDB release 9.4, prior to inclusion of the ChIP data used here, with overlapping or

780 bookended sites for the same TF merged prior to analysis); data are from [26] (Lrp ChIP) or the present study (IPOD-HR). Data are taken from the most closely equivalent conditions (log phase growth in minimal media, log phase growth in rich media, stationary phase in rich media),

785

790 although the carbon source is different (glycerol vs. glucose). **(C)** Heat map showing the  
consensus clustering (co-occurrence frequencies) of the pattern of occupancy dynamics for the  
regulons of all considered TFs across the varied nutrient conditions in this study (see Methods  
for details). Consensus division into ten clusters via agglomerative clustering is shown at right;  
for each cluster, representative TFs (on matrix) and regulated gene ontology terms (right) are  
shown, with numbers in parentheses indicating the approximate p-value for enrichment of that  
GO term. A full listing of p values is given in **Table S4**. **(D)** Changes in occupancy and target  
795 gene transcript level for all annotated repressive binding sites of ArgR and PurR (for minimal  
media vs. rich media), in each case demonstrating the strong and oppositely directed changes  
in binding and regulatory effects across the regulons. **(E)** Correlation of promoter-level  
occupancy changes (measured by RNA polymerase ChIP-seq) and changes in transcript  
abundance, shown for the WT stationary phase condition compared with exponential phase.  
800 Shaded area shows a bootstrap-based 95% confidence interval. **(F)** IPOD-HR protein  
occupancy profiles in the vicinity of the *potF* promoter under the indicated conditions. Drawn TF  
binding sites are taken from Ecocyc [54] reflecting recent updates in known TFBSs in this  
region. **(G)** IPOD-HR occupancy profiles upstream of *ndh* under the indicated conditions. For all  
rows of TFBSs except the top, all TFBSs in a given row correspond to the factor named at the  
805 beginning of that row.



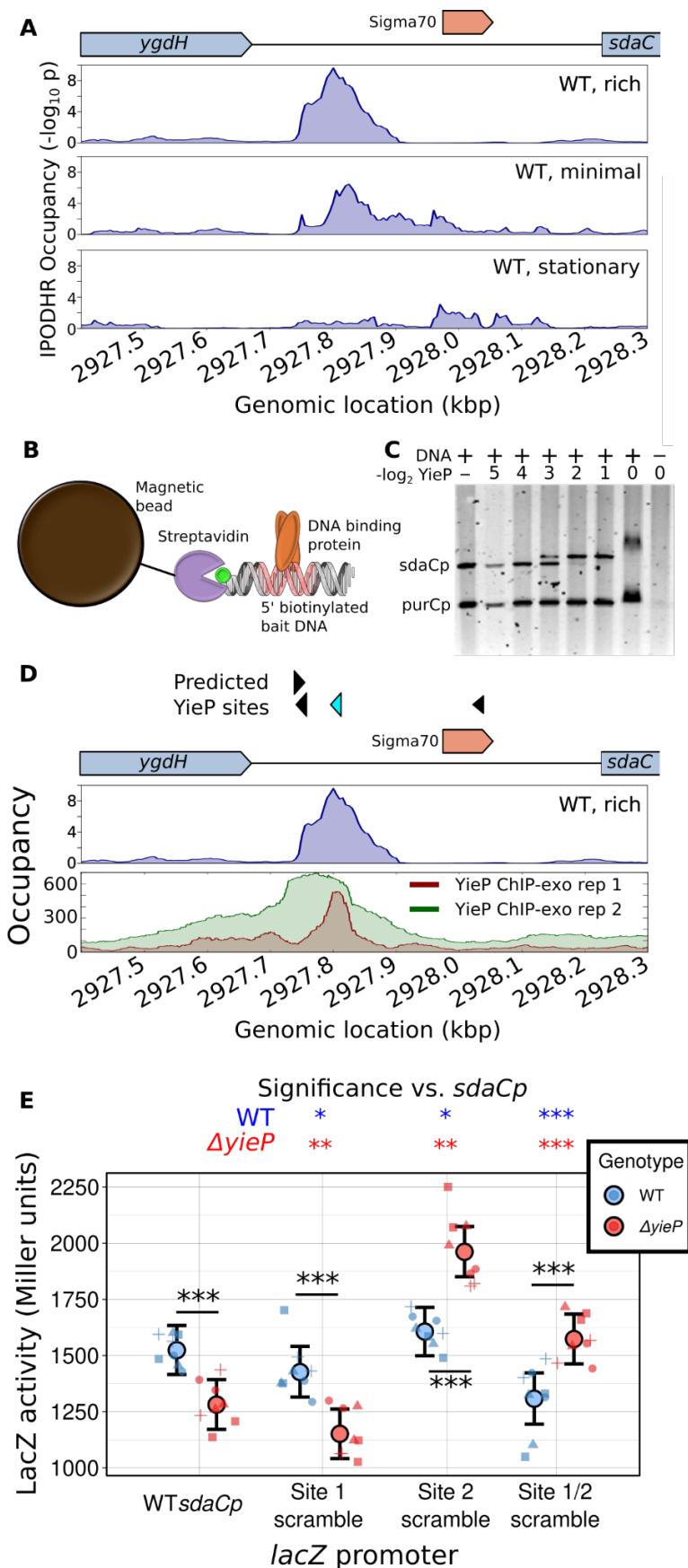


**Figure 4: Experimental identification of the protein bound to a novel occupancy peak upstream of the *sdaC* promoter.** (A) IPOD-HR profiles upstream of *sdaC* in rich (M9/RDM/glu) media, minimal (M9/glu) media, and in rich media in stationary phase. (B) Schematic of pulldown/mass spectrometry experiments used to identify factors binding the *sdaC* promoter. (C) Gel shift experiments showing specific interaction of YieP with the *sdaC* promoter. Increasing concentrations of purified His<sub>6</sub>-YieP are incubated with a mixture of fluorescein-labeled promoter regions from *sdaC* and *purC* and then run on a gel, demonstrating specific shifting of the *sdaC* promoter region. YieP concentrations are given as the number of two-fold dilutions relative to full strength. (D) Comparison of IPOD-HR occupancy profile (as in panel A) with ChIP-exo data from [30], with the latter given as total read counts (parsed from GEO accessions GSM3022131 and GSM3022132). The top track of predicted YieP sites shows significant hits for the YieP motif identified based on that ChIP-exo data set. Out of 1,025 potential YieP sites in the genome, the location highlighted in cyan is tied for 10th highest score (identified using FIMO; see Methods for details). Occupancy signal is given as  $-\log_{10}(p)$  for the IPOD-HR track, or raw counts (averaged across strands) for the ChIP-exo tracks. (E) Results of Miller assays in which *lacZ* transcription is driven by a copy of the *sdaC* promoter, either with the native sequence (WT) or with one or both of the apparent YieP binding sites scrambled, in both a WT and *yieP* background. Large points and error bars show a posterior mean and 95% credible interval from a Bayesian analysis; small points show individual data points, with symbols denoting the day on which data were gathered (a total of 8 biological replicates split across four different days were performed for each strain). Significance is assessed using one-sided Bayes factors with the interpretive scale of Kass and Raftery [55] (\*: Substantial, \*\*: Strong, \*\*\*, Decisive). Stars within the plot denote direct comparisons of the WT and *yieP* strains for each promoter, whereas those above the plot denote comparisons of each promoter variant with the original within a given genetic background.

835

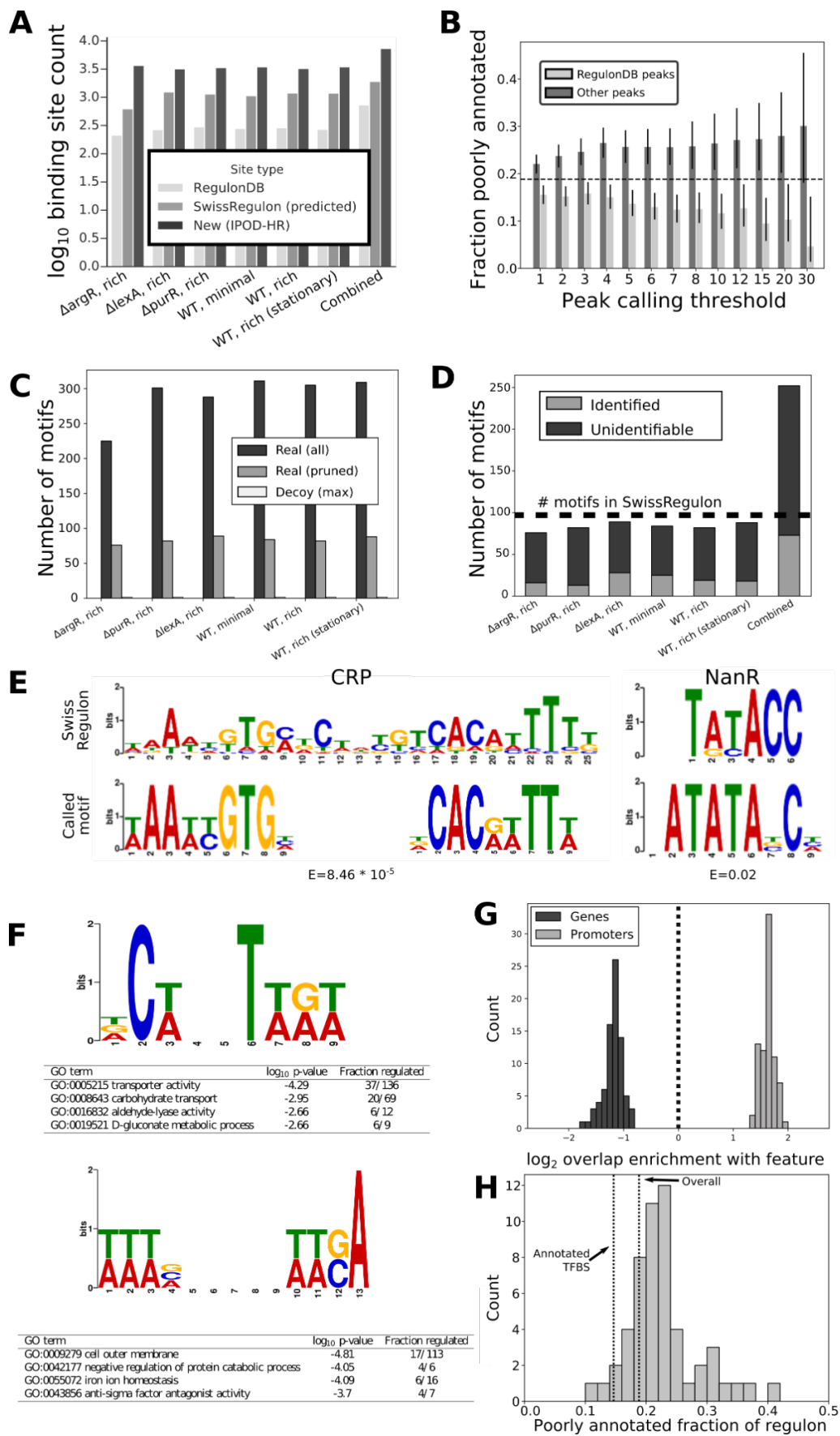


**Figure 5: Genome-wide *de novo* discovery of sequence specificity motifs for actively bound transcription factors.** (A) At a peak calling threshold of 4 (c.f. **Figure S1**), we show the number of identified binding sites that overlap with annotated sites in RegulonDB (“RegulonDB”), motif-based predicted binding sites (“SwissRegulon”), or novel (“New”). The “Combined” category represents peak sets where the peaks at a given threshold identified across all conditions are merged, prior to comparisons with the RegulonDB and predicted databases. Qualitatively similar results are observed at all tested peak calling thresholds (data not shown). (B) All called IPOD-HR occupancy peaks across the conditions shown in panel A were combined, and then partitioned based on whether they overlap with a known or inferred binding site in RegulonDB (RegulonDB peaks) or not (Other peaks). Peaks were then considered to have regulatory potential if they fell within 100 bp of an annotated transcription start site, and the fraction of the genes potentially regulated by each peak category plotted across different peak calling threshold. Error bars show 95% credible intervals calculated assuming that the incidence of poorly annotated genes in the inferred regulon is a binomial random variable, using Bayesian inference with a Beta(1,1) prior. The dashed line shows the overall fraction of poorly annotated genes included in the analysis (that is, those belonging to transcripts regulated by at least one annotated transcription start site in RegulonDB). (C) Number of motifs discovered *de novo* using IPOD-HR occupancies under each condition in our study. “All” and “pruned” refer to all discovered motifs and those surviving cluster-based filtering by RSAT (see Methods for details), respectively. “Real” shows the motif counts discovered in real data, and “Decoy” shows the maximum discovered motif count across 20 independent circular permutations of the data under each condition. (D) Classification of non-redundant motifs across conditions as “Identified” (match to an existing motif from the SwissRegulon database, via TOMTOM, with E-value < 0.5) or “Unidentified” (no matches found with E<0.5). “Combined” refers to the full set of motifs discovered after pooling all motifs across all conditions and redundancy filtering; a horizontal dashed line shows the total number of known motifs present in SwissRegulon. (E) Example cases of “Identified” matches of IPOD-HR-inferred motifs with motifs from the SwissRegulon database, showing good correspondence with annotated CRP (left) and NanR motifs. E values arising from the TOMTOM search pairing newly discovered motifs with similar known motifs are shown beneath each inferred motif. y axes for motifs in this and the following panel show information content in bits. In the case of CRP, the half site was inferred, and is shown here in both the forward and reverse orientations aligned to the motif in SwissRegulon. (F) Examples of two newly inferred motifs that do not have identifiable hits in the SwissRegulon database (as assessed using TOMTOM). In each case, the gene ontology (GO) terms showing most significant enrichments amidst the predicted regulon associated with that motif are shown (see Methods for details). (G) Overlap of predicted binding sites for IPOD-HR inferred motifs with either coding regions (genes) or promoters (both as annotated in RegulonDB) using only strict motif hits; shown are the log<sub>2</sub> fold enrichment or depletion of the overlap as compared with that expected by chance. (H) For the predicted regulon of each newly inferred motif (using only strict motif hits), we show the fraction of regulon members that are poorly annotated (Uniprot annotation score of 1 or 2 out of 5); for comparison, dashed lines are shown for the values obtained when the same statistic is calculated for all annotated TF-gene interactions in RegulonDB (“Annotated TFBS”), and for the genome as a whole (“Overall”).

885

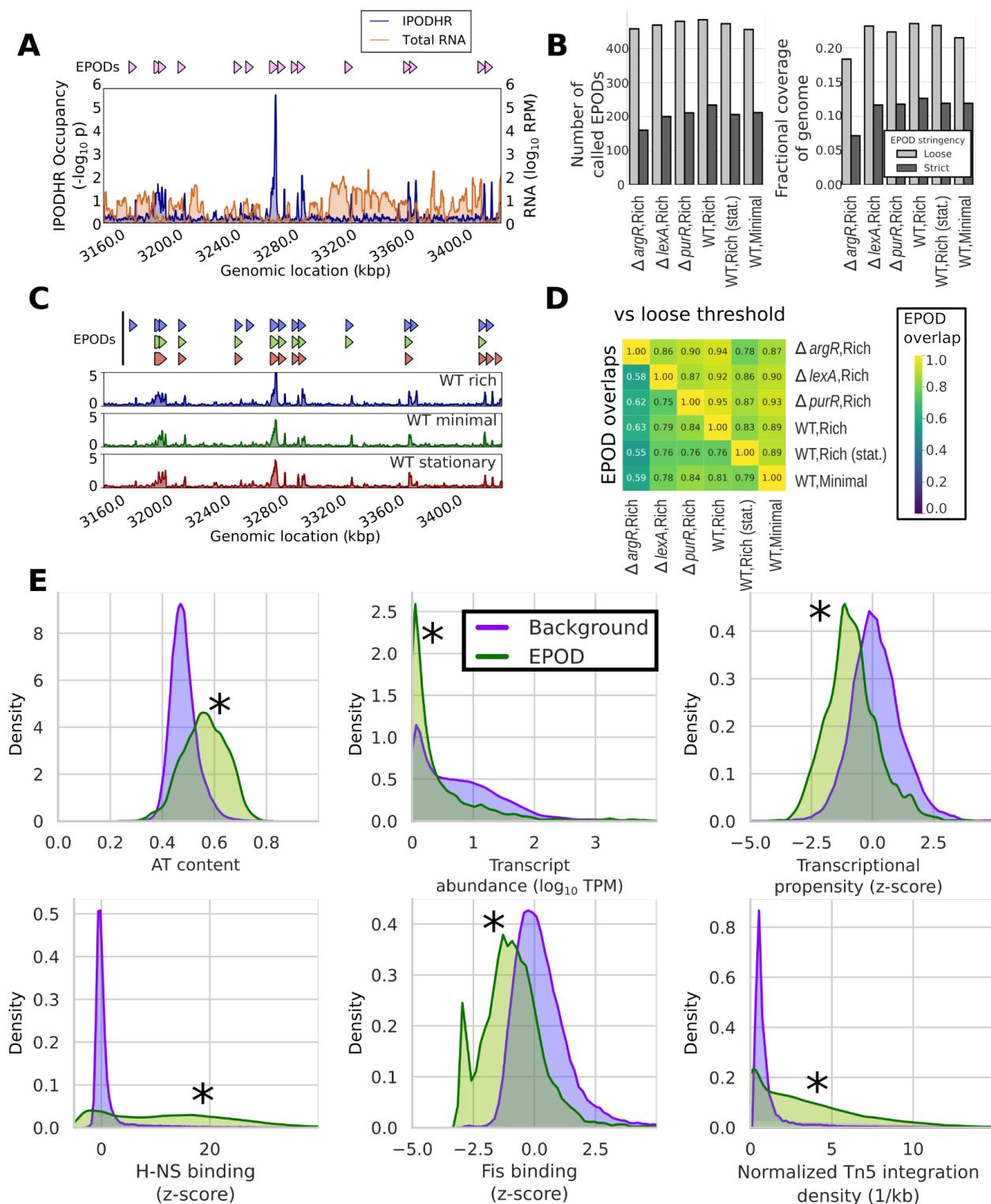
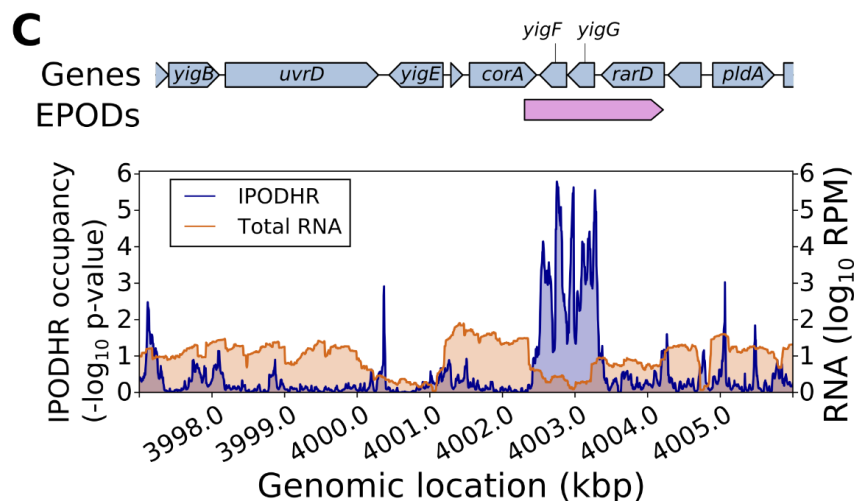
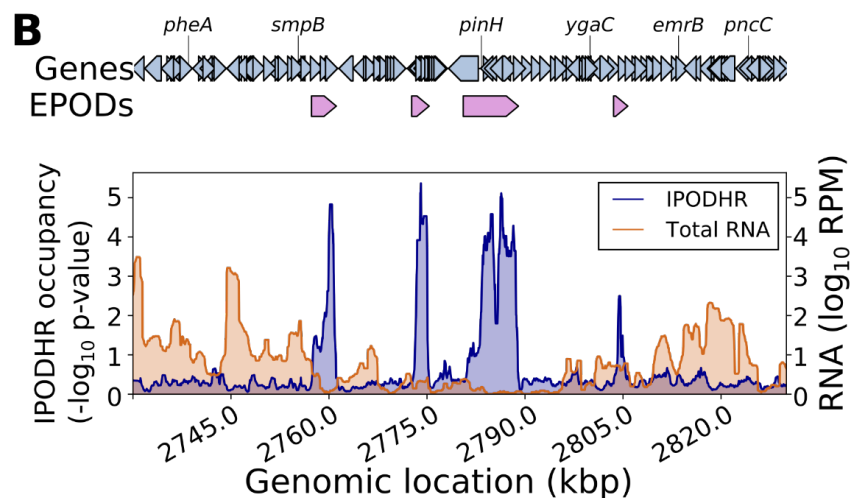
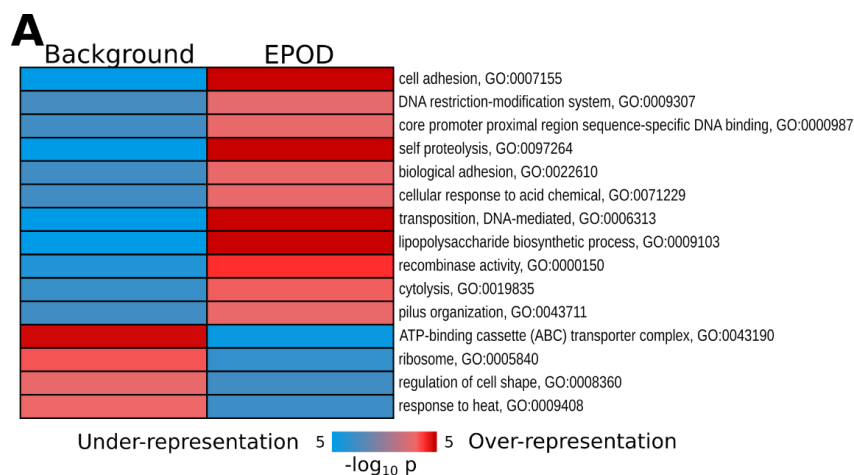


**Figure 6: EPODs define stable genomic structures and are associated with many distinct features. (A)** EPOD calls from a representative genomic region in the WT Rich media condition, along with protein occupancy and RNA levels smoothed with a 1 kb rolling median. All

890

displayed/analyzed EPOD calls refer to our strict threshold unless otherwise noted. **(B)** Number of called EPODs by condition (left) and fraction of the genome covered by EPODs (right) for both our loose and strict thresholds (see text for details). **(C)** IPOD-HR occupancies (shown over a 1 kb rolling median) and associated EPOD calls under three different conditions, in the same genomic region shown in panel **A**. EPOD calls are shown above the occupancy, in the same order as the data tracks. **(D)** Lower triangle: Overlap of EPOD calls (using a symmetrized distance that is the average of the fraction of EPOD positions from a condition *a* that is also called in condition *b*, and *vice versa*) between each pair (*a,b*) of the studied conditions. Upper triangle: each entry shows the fraction of the EPOD calls (at a 5 bp resolution) from the sample defining that row that is contained in a relaxed set of EPOD calls (see text) of the sample defining that column (only the upper triangle of that matrix is shown). **(E)** Density plots showing normalized histograms (smoothed by a kernel density estimator) of the specified quantities for regions of the genome that are in EPODs versus those that are not (Background), as assessed in the WT M9/RDM/glu (WT, rich) condition. “\*” indicates FDR-corrected  $p < 0.005$  via a permutation test (against a null hypothesis of no difference in medians). Significance calling and additional comparisons are shown in **Table S3**.



910

**Figure 7: EPODs are statistically enriched for genes in specific functional categories.** (A) The genome was split into EPOD and background regions as in Figure 6; we then applied iPAGE [35] to identify gene ontology terms showing significant mutual information with occupancy in EPODs. All shown GO terms were significant according to the built-in tests in

915 iPAGE. **(B)** Multiple EPODs are associated with silencing of the CP4-57 prophage. Shown are the IPOD-HR occupancy and transcript levels in the vicinity of the prophage locus during growth in rich defined media with glucose, with EPOD locations indicated above the plots. **(C)** Association of a small EPOD with two genes of unknown function, *yigF* and *yigG*, along with the putative transporter *rarD/yigH*; data tracks defined as in panel **B**.



## 920 Methods

### Strain construction

The base strain for all experiments used here is an MG1655 stock obtained from the Tavazoie lab, which belongs to the substrain typified by ATCC 700926 [56]. All specified gene knockouts were obtained by P1 transduction [57] of the FRT-flanked *kanR* marker from the corresponding  
925 knockout strain of the Keio collection [58], followed by Flp recombinase mediated excision of the marker using the pCP20 plasmid [59] to leave a small scar in place of the original open reading frame. Candidate isolates for each deletion were grown overnight at 42° C to drop the pCP20 plasmid, and then replica plated onto appropriate selective plates to ensure loss of both the plasmid and kanamycin resistance marker. Knockouts were confirmed by PCR fragment sizing  
930 and/or sequencing across the marker scar. Note that the  $\Delta lexA$  strain that we refer to is in fact  $\Delta lexA/\Delta sulA$ , as loss of *lexA* is lethal in the presence of a functional *sulA* gene [60,61].

For construction of the *lacZ* reporter strains for the experiments shown in **Figure 4E**, the *lacZ* gene from our MG1655 background strain was first removed by P1 transduction of a  
935 chloramphenicol resistance gene, yielding MG1655 *lacZ::cml*. An additional copy of this strain was constructed by transduction of the Keio collection *yieP::kan* gene and subsequent marker excision (as above) to yield MG1655 *lacZ::cml yieP::scar*. We then generated plasmid-born copies of a reporter gene in which the *lacZ* open reading frame was placed directly after the *sdaC* promoter of *E. coli* MG1655 (positions 2927672-2928228 on the U00096\_3 reference  
940 genome). We also generated promoter variants in which either or both of the identified putative YieP binding sites in the promoter were perturbed, with Site 1  
“catttcAT**TTG**TTATATGA**AAT**gtttcctt” to “catttcAT**AAC**TTATATG**TTA**gtttcctt” containing a mutation and Site 2 containing a “cagttaAT**ATG**TCATAC**AATT**tatggttg” to  
“cagttaAT**GAC**TCATAC**TTCA**tatggttg” mutation (in each case the capitalized region is the  
945 putative YieP site; Site 2 corresponds to site highlighted in cyan in **Fig. 4D**, with Site 1 the site further upstream of it relative to *sdaC*). All four promoter variants were generated by Gibson assembly [62] using the NEB Hifi Builder Master Mix on a plasmid next to an FRT-flanked kanamycin resistance marker, cloned into DH5 $\alpha$  cells, and validated by Sanger sequencing of the promoter and adjacent plasmid regions. The promoter-*lacZ* constructs were then each  
950 integrated into a WT MG1655 strain replacing the *araC-araBAD* locus via  $\lambda_{red}$  recombination of a dsDNA PCR product produced using NEB Q5 polymerase (using pKD46 as a helper plasmid as above), selected on MacConkey/arabinose + kanamycin plates, and transduced into the MG1655 *lacZ::cml* and MG1655 *lacZ::cml yieP::scar* strains. The kanamycin resistance marker was removed following the standard pCP20-based marker excision protocol as above, and the  
955 final eight strains (all pairwise combinations of four promoter variants and *yieP*<sup>+/-</sup>) were validated by PCR fragment sizing of the *yieP* and *ara* loci, and Sanger sequencing of the *sdaC* promoter at the *ara::sdaCp-lacZ* locus.

## Media/culture conditions

960 For routine cloning applications and for recovery of cryogenically preserved cells, we used LB (Lennox) media (10 g/L tryptone, 5 g/L yeast extract, 5 g/L NaCl), with bacteriological agar (15g/L) added as appropriate.

965 For physiological experiments, we made use of a variety of supplemented versions of M9 defined medium (6 g/L Na<sub>2</sub>HPO<sub>4</sub>, 3 g/L KH<sub>2</sub>PO<sub>4</sub>, 1 g/L NH<sub>4</sub>Cl, 0.5 g/L NaCl, 1 mM MgSO<sub>4</sub>) [57]. Our M9 minimal media condition (M9/min) additionally includes 0.2% (w/v) glucose, 0.4 mM CaCl<sub>2</sub>, 40 μM ferric citrate, and the micronutrient mixture typically incorporated in MOPS minimal media [63]. Our M9 rich defined medium condition (M9/rdm) instead incorporates into the M9 base 0.4% (w/v) glucose, MOPS micronutrients (as above), 4 μM CaCl<sub>2</sub>, 40 μM ferric citrate, and 1x supplements ACGU and EZ as used in MOPS rich defined medium [63].

## 970 Cell growth and harvest for IPOD-HR

The cells of interest were grown overnight in the media of interest after inoculation from an LB plate. In the morning, the culture was back-diluted into fresh, prewarmed media to an OD<sub>600</sub> of 0.003. The culture was then grown to the target OD<sub>600</sub> (0.2, except in the case of stationary phase samples, which are described below), at which point a 200 μL aliquot was removed and 975 preserved in 1 mL of DNA/RNA Shield (Zymo Research) following the manufacturer's instructions.

The remainder of the culture was treated with rifampin to a final concentration of 150 μg/mL, and incubated for 10 minutes under the same culture conditions as the main growth to 980 immobilize initiating RNA polymerase at active promoters and permit completion of transcripts in progress. The culture was then rapidly mixed with concentrated formaldehyde/sodium phosphate (pH 7.4) buffer sufficient to yield a final concentration of 10 mM NaPO<sub>4</sub> and 1% v/v formaldehyde. Crosslinking was allowed to proceed for 5 minutes at room temperature with vigorous shaking, followed by quenching with an excess of glycine (final concentration 0.333 M) 985 for 5 minutes with shaking at room temperature. The crosslinked cells were subsequently chilled on ice, and washed twice with ice cold phosphate buffered saline, 10 mL per wash. The fully washed pellets were carefully dried, any remaining media pipetted away, and then the pellets were snap-frozen in a dry ice-ethanol bath and stored at -80 C.

990 In the case of our stationary phase samples, cells were grown as described above in terms of back-dilution and growth to an OD<sub>600</sub> of 0.2, and then grown for an additional three hours prior to RNA harvest, rifampin treatment, and crosslinked as described above.

## Cell lysis and DNA preparation

995 Frozen cell pellets were resuspended in 1x IPOD lysis buffer (10 mM Tris HCl, pH 8.0; 50 mM NaCl) containing 1x protease inhibitors (Roche Complete Mini, EDTA free) and 52.5 kU/mL of ready-lyse (Epicentre); 600 μL per pellet (stationary phase cells were diluted 10x prior to lysis, and only 1/10 of the resulting material used, due to the much higher biomass of those pellets).

1000 We incubated the resuspended pellet for 15 minutes at 30 C, and then placed it on ice. We then  
sonicated the cells using a Branson digital sonicator at 25% power, using three 10 second  
bursts with 10 second pauses between bursts. The cells were maintained in a wet ice bath  
throughout sonication.

1005 We then performed a calibrated DNA digestion to sub-200 bp fragments, by adding to the  
sonicated lysates 60 µg RNase A (Thermo Fisher), 6 µL DNase I (Fisher product #89835), 5.4  
µL 100 mM MnCl<sub>2</sub>, and 4.5 µL 100 mM CaCl<sub>2</sub>, and then incubating on ice. While the  
appropriate digestion time must be calibrated for each particular sample type and batch of  
DNase, 30 minutes of digestion proved appropriate for all samples here. Reactions were  
quenched after completion by the addition of 50 µL 500 mM EDTA (pH 8.0), typically yielding  
50-200 bp fragments.

1010

### IPOD-HR Interface Extraction

1015 Prior to interface extraction, samples were clarified by centrifugation for 10 minutes at  
16,9000xg at 4° C. After clarification, a 50 microliter input sample was diluted 1:9 in elution  
buffer (50 mM Tris, pH 8.0; 10 mM EDTA; 1% SDS) and kept on ice until the reverse  
crosslinking step. The remainder of the lysate was mixed with 1 volume of 100 mM Tris base  
and 2 volumes of 25:24:1 phenol:chloroform:isoamyl alcohol, vortexed, and then incubated for  
10 minutes at room temperature. After incubation, the sample was spun at 21,130xg for two  
minutes at room temperature, allowing formation of a white disc at the aqueous-organic  
interface enriched for protein-DNA complexes [10,11].

1020

1025 The complete aqueous phases were removed and discarded, and the remaining disc washed  
again with 350 microliters TE (10 mM Tris, pH 8.0; 1 mM EDTA), 350 microliters 100 mM Tris  
base, and 700 microliters 24:1 chloroform:isoamyl alcohol. The resulting mixture was vortexed  
vigorously, and again centrifuged for 2 minutes at 21,130xg. All liquid was again removed, and  
the wash was repeated using 700 microliters TE and 700 microliters 24:1 chloroform:isoamyl  
alcohol. After vortexing, centrifugation, and removal of the final wash (exactly as above), any  
residual liquid was removed by wicking with a laboratory wipe (if any substantial pools of liquid  
were present). Finally, the interface was resuspended in 500 microliters of elution buffer  
(described above), vortexed vigorously, and kept on ice until reverse crosslinking (no more than  
a few hours).

1030

1035 We caution the reader that the separation of the interface layer from the liquid on either side of it  
is crucial to success with this method. We have found it most effective to tilt the microcentrifuge  
tube toward while pipetting out the organic layer from beneath, at which point the interface will  
adhere to the tube wall and allow easy removal of the aqueous layer. We have also found that  
the handling characteristics of the interface vary greatly with the plasticware in use. For the work  
described here, we have used 2 mL microcentrifuge tubes from USA Scientific for all interface  
handling, as the interfaces adhere nicely to the tube wall (other plasticware may yield variable  
results); at the same time, the use of low-retention pipette tips appears to reduce binding of the  
interface to the tip.

1040

## RNA polymerase chromatin immunoprecipitation

DNA for RNA polymerase ChIP-seq experiments was prepared as described above for IPOD-HR interface extraction up through the lysate clarification stage. Whenever possible, we used frozen pellets obtained from the same culture for matched IPOD-HR and ChIP-seq experiments, in which case the lysates were pooled and mixed immediately prior to removal of a single input sample. ChIP procedures here were modeled on those of [64].

The digested lysates were mixed 1:1 with 2x IP buffer (200 mM Tris, pH 8.0; 600 mM NaCl; 4% Triton X-100; 2x Roche Complete EDTA-free protease inhibitors), and then kept on ice for no more than a few hours prior to antibody addition. We added 10 microliters of purified anti-*E. Coli* RNA polymerase antibody (Neoclone WP023), and incubated overnight with rocking at 4 C. Near the end of the incubation period, we resuspended an aliquot of 50 microliters of protein G dynabeads (Invitrogen) and equilibrated the protein G beads with 1x IP buffer lacking protease inhibitors. The bead aliquot was added to the antibody-lysate mixture, and then incubated 2 hours with rocking at 4° C. The bead-antibody-target complexes were subsequently subjected to the following series of washes, with 1 mL used per wash. All washes were at room temperature, and involved manual resuspension of the beads in the new wash buffer followed by immediate re-separation.

- 1x Wash buffer A (100 mM Tris, pH 8.0; 250 mM LiCl; 2% Triton X-100; 1 mM EDTA)
- 1x Wash buffer B (100 mM Tris, pH 8.0; 500 mM NaCl; 1% Triton X-100; 0.1% sodium deoxycholate; 1 mM EDTA)
- 1x Wash buffer C (10 mM Tris, pH 8.0; 500 mM NaCl; 1% Triton X-100; 1 mM EDTA)
- 1x TE (10 mM Tris, pH 8.0; 1 mM EDTA)

The antigens were subsequently eluted by adding 500 microliters of elution buffer (composition described above) and incubating 30 minutes at 65° C, with vigorous vortexing every 5-10 minutes.

## Crosslinking reversal and recovery of DNA

The DNA from the input, IPOD-HR, and ChIP fractions described above was recovered using identical procedures: samples diluted in elution buffer (see above) were incubated overnight (6-16 hours) at 65° C to reverse formaldehyde crosslinks. After allowing the samples to cool to room temperature, we then added 100 µg of RNase A (Thermo-Fisher), incubated 2 hours at 37° C, then added 200 µg of proteinase K (Fermentas) and incubated an additional 2 hours at 50° C. DNA was then recovered via standard phenol-chloroform extraction and ethanol precipitation, following protocols from [57]. We used Glycoblue (Ambion) as a co-precipitant, NaCl as a precipitating salt (due to the presence of SDS in our solution), and washed with ice-cold 95% ethanol to avoid loss of low molecular weight DNA.

Recovered DNA was quantified via fluorescent quantitation (using either the Invitrogen PicoGreen or Promega QuantIT system), and samples of sufficiently high concentration were also run on a 2% agarose gel for fragment size assessment. Typical total yields from the procedure above were on the order of 1 µg of DNA for the input samples, 100-200 ng for the IPOD-HR samples, and 1-10 ng for the ChIP samples.

## Preparation of next-generation sequencing (NGS) libraries

1085 Except as otherwise noted, all DNA samples were prepared for Illumina sequencing using the NEBNext Ultra DNA Library Prep Kit (NEB product #E7370), with either single index or dual index primers also obtained from NEB. We followed the manufacturer's instructions except for the following variations:

- 1090 • Cleanups prior to adapter ligation were performed using a Zymo Clean&Concentrator 5 spin column kit or Zymo Oligo Clean&Concentrator spin column kit instead of Ampure beads, in order to avoid the loss of low molecular weight DNA
- We used Ampure and Axygen PCR cleanup beads interchangeably, having established in side-to-side comparisons that they were functionally identical for the steps in the NEB sequencing prep (data not shown). The final cleanup step was in some cases repeated to remove obvious populations of adapter dimers.

1095 All libraries were sequenced on either an Illumina HiSeq or NextSeq instrument; detailed statistics on read lengths and counts are provided in **Table S5**. A small number of samples were prepared for sequencing using an Illumina Truseq Nano kit or (in the case of one biological replicate) a Truseq kit instead of the NEBnext kit noted above (those samples are identified in  
1100 **Table S5**); we found that upon calculation of correlations between the coverages of a broad range of IPOD, input, and RNA polymerase ChIP-seq samples prepared using various sequencing preparation kits that the Truseq Nano samples were indistinguishable from NEBNext Ultra samples upon clustering of the occupancy profiles across sample types and conditions. To avoid any possibility of bias from the single included Truseq replicate (which was  
1105 for the  $\Delta lexA$  genotype), we observed qualitatively equivalent results in TFBS occupancy dynamics (**Fig. 3A**) if the Truseq replicate was removed from analysis (data not shown).

## RNA isolation and RNA-seq sample preparation

As noted above, samples for RNA isolation were preserved immediately prior to rifampin addition by dilution in a 5x excess of DNA/RNA Shield (Zymo); the RNA samples were then  
1110 stored at -80° C until purification. RNA was isolated using a Zymo QuickRNA microprep kit following the manufacturer's instructions, including the on-column DNase digestion. Purified RNA was quantified using RiboGreen (Invitrogen), and then ribosome-depleted using the Illumina RiboZero Gram-negative bacteria kit according to the manufacturer's instructions, with the input RNA amount and all reaction volumes cut in half. Final recovery of the ribo-depleted  
1115 RNA was accomplished using the modified Zymo spin column protocol present in the RiboZero documentation. Ribo-depleted RNA was then prepared for sequencing using the NEBNext Ultra Directional RNA kit (NEB product E7420), and sequenced as described above for the DNA samples.

## 1120 Analysis of NGS data

All NGS data was preprocessed using a common pipeline, after which DNA and RNA data sets were processed separately. The reference genome in all cases was the most recent version of

1125 the *E. coli* MG1655 genome (GenBank U00096.3), with gene, transcription factor binding site,  
and transcription start site annotations from RegulonDB [7]. Data processing was automated  
using in-house python and bash scripts, and parallelized where possible using GNU parallel [65]  
or the python `multiprocessing` library. The python and bash source code used to derive  
processed occupancy data from raw reads is available from [https://github.com/freddolino-lab/ipod\\_v1\\_2020](https://github.com/freddolino-lab/ipod_v1_2020); we also have distributed a ready-to-use analysis environment in the form of a  
singularity container, as documented in the github repository noted above.

1130

### Read Quality Control and Preprocessing

All reads were subjected to adapter removal using cutadapt 1.8.1 [66] to cut the common  
sequence of Illumina Truseq adapters, and then trimmed to remove low-quality read ends with  
Trimmomatic 0.33 [67], using the trimming steps 'TRAILING:3 SLIDINGWINDOW:4:15  
1135 MINLEN:10'. Samples were subjected to additional manual quality checks using FastQC [68]  
and MultiQC [69] to identify any irregularities in terms of sequence content, quality, or  
duplication.

### DNA Sequencing and Protein Occupancy Calling

1140 Surviving DNA reads were aligned to the U00096.3 genome using bowtie2 version 2.1.0 with  
"very sensitive" end-to-end alignment presets, and dovetail alignments allowed. Only  
concordant paired-end reads were retained for subsequent quantitation. Read occupancies  
were calculated at a 5 bp resolution along the chromosome using the parsing method of Kroner  
*et al.* [26], and scaling the basepair-wise contribution of each read by the inverse of its length  
1145 (thus, each read contributed the same total amount of occupancy signal). The resulting read  
densities were then quantile normalized, acting separately for the input, IPOD interface, and  
RNA polymerase ChIP-seq tracks of each biological condition. In order to account for the  
higher amount of genomic DNA present near the origin of replication relative to the terminus, we  
fitted a smoothing spline with four evenly spaced knots and periodic boundary conditions to the  
1150 input sample for each condition; the smoothing spline provides a low-pass filter on abundances  
that accounts for large-scale variations in DNA abundance across the genome. The use of four  
knots allows inflection points at the origin, terminus, and the halfway points between them. All  
occupancy datasets were divided by the spline-smoothed abundances of the corresponding  
input data prior to further processing. After abundance normalization, all data tracks were  
1155 rescaled to have matching means, and then all replicates for each sample type/biological  
condition combination were averaged to generate a composite occupancy track (yielding, for  
example, one input data track for the WT M9/RDM/glu condition, one IPOD data track for the  
WT M9/RDM/glu condition, etc.).

1160 The displayed IPOD and ChIP data tracks were then obtained as  $\log_2$  ratios of the extracted  
(interphase or ChIP) to input samples for each condition; we refer to these tracks as the "IPOD"  
and "ChIP" signals below. Upon viewing the correlation between total protein occupancy and  
RNA polymerase occupancy, two protein-occupied subpopulations were apparent (**Figure S5**):  
a linear subpopulation where total protein and RNA polymerase are well-correlated, and a  
1165 second subpopulation of positions where the total protein occupancy is much higher than  
expected based on the RNA polymerase occupancy. We interpret the former set of positions as

protein occupancy due directly to RNA polymerase binding, and the latter as non-RNA polymerase occupancy (as schematized in **Fig. 1B**). To obtain the fully processed IPOD-HR signal for non-RNA polymerase occupancy, we applied a modified linear model to estimate and then remove the contributions of RNA polymerase to the observed signal. To this end, we began by using only the top 2% of observed ChIP values, which are presumed to represent sites that are bound entirely by RNA polymerase in the IPOD vs. ChIP signal comparison (as in **Fig. S5**). We then generated the line with the lowest possible slope, and zero intercept, that is sufficient to keep 95% of the high-ChIP data region below it; thus, this represents a linear transformation of the ChIP signal that is sufficient to remove the vast majority of RNA polymerase occupancy. The resulting slope of the IPOD vs. ChIP data was then used to generate a prediction of the IPOD contribution attributable to RNA polymerase binding at each position based on the observed ChIP signal itself, and that value subtracted from the IPOD signal. No subtraction was performed at positions where the observed RNA polymerase occupancy was negative, so that the ChIP subtraction can only lower (not raise) occupancy. We note that the choice of slope to completely eliminate all occupancy at 95% of the high-ChIP sites represents a highly conservative choice (in terms of removing virtually all occupancy from the IPOD signal that could potentially be attributed to RNA polymerase). Any choice for this parameter must necessarily reflect a balance of risks, where lower values (close to 50%, which would roughly match a direct linear fit to the IPOD vs. ChIP data points) increase the odds of identifying spurious protein occupancy peaks actually attributable to RNA polymerase, and higher values (up to 100% would be conceivably justifiable) risk erasing true regulatory protein occupancy due to overzealous RNA polymerase occupancy removal.

We refer to the resulting ChIP-subtracted IPOD signal as the IPOD-HR signal; for analysis and display we further standardize the signal by calculating robust z scores, where the robust z-score  $z_i$  at position  $i$  is defined as

$$z_i = (x_i - \text{median}(\mathbf{X})) / \text{mad}(\mathbf{X})$$

for a IPOD-HR data vector  $\mathbf{X}$ , and  $\text{mad}()$  indicates the median absolute deviation. In many cases a more useful signal for visualization is a p-value for enrichment at each site;  $\log_{10}$  p-values are calculated under the null hypothesis that the distribution of the robust z-scores is standard normal. To provide uncertainty estimates grounded in observed levels of biological variability across replicates, for each data point we also constructed an interval between the lowest and highest values that could have been obtained for our occupancy statistics using any combination of biological replicates (potentially different replicates for the IPOD, ChIP, and input samples to construct the largest possible range). To calculate the error bars shown in Figure 3A, we then used parametric bootstrapping to generate confidence intervals for the parameters of interest, assuming that the  $\log_{10}p$  scaled occupancy of each TFBS followed a log-normal distribution with a mean of the observed mean and standard deviation of one-quarter the range between the highest and lowest replicate-wise values (thus treating the range of the pessimistic replicate-wise possible values as an interval expected to contain ~95% of observed points); 95% confidence intervals for the average site-wise occupancies were then calculated from 1,000 bootstrap replicates.

## Feature calling

1215 To identify peaks in the robust z-scaled IPOD-HR data, we applied continuous wavelet  
transform (CWT) peak calling [70] (as implemented in the `scipy.signal` package), with a range of  
widths from 25 bp to 125 bp (at 5 bp increments, reflecting the expected range of peak sizes  
given the fragmentation of our input DNA) used to generate the CWT matrix, and refer to peaks  
based on the minimum signal-to-noise ratio threshold at which they appear as peak calls (note  
1220 that in the CWT method, a range of widths must be specified as part of the algorithm, and gives  
rise only to a single peak set). To provide quantitative measures of the evidence for different  
peak calls, separate peak sets were generated at several signal to noise thresholds (a full listing  
can be observed in the set of thresholds shown in **Supplementary Data S2**). Each peak call  
was padded by 30 bp on each side to define the peak region used in subsequent analysis. We  
1225 show the performance of a variety of calling thresholds in identifying known TFBSs in **Figure  
S1**, and based on those findings, use a threshold of 4 for all other quantitative analysis  
presented here. However, peak sets at all thresholds are supplied in **Supplementary Data S2**.  
Comparisons were made to data from RegulonDB release 9.4 unless otherwise noted.  
Extended protein occupancy domains (EPODs) were called using an approach similar to that in (Vora et  
1230 al., 2009): we identified EPOD seed regions as any region at least 1,024 bp in length, over which a 512 bp  
rolling median exceeded the overall  $k$ th percentile of a 256 bp rolling median across the entire  
chromosome (in all cases acting on the robust z-scored IPODHR data); we used  $k=90$  for the main EPOD  
calls made in the text, and  $k=75$  for the relaxed version used in threshold analysis. In the case of  
overlapping seeds, only the one with the highest median was retained. Seed regions were then  
1235 expanded in both directions as far as possible while maintaining the median over the entire  
EPOD call above the threshold noted above, and without crossing any location with a robust z-  
score  $\leq 0$ . We note that the lower threshold ( $k=75$ ) matches the original EPOD definitions from (Vora  
et al., 2009), whereas the more stringent threshold is intended to highlight the most robust regions of  
large-scale protein occupancy; both thresholds show similar properties in terms of overlaps with gene  
1240 sets and genomic features.

## Transcription factor co-clustering analysis

1245 For the transcription factor occupancy and co-clustering data, we performed consensus  
clustering (inspired by [71]). For each biological condition, we assigned each transcription factor  
a score given by the geometric mean of the site-level occupancies (IPOD-HR  $-\log_{10}$  p values) for  
annotated binding sites of that TF in that condition (using a minimum value of 0.01 for each site-  
level value); the condition-wise average occupancies for each TF were then divided by the  
highest average occupancy for that TF across all conditions, yielding an occupancy score on the  
1250 interval (0,1] for each TF-condition combination. The occupancy profiles of TFs across  
conditions were clustered 100 times using K-means clustering at each number of clusters



1255 between 8 and 12 (inclusive); the ‘co-clustering frequency’  $\kappa$  is defined as the fraction of those 100 trials in which a given pair of TFs were assigned to the same cluster. We then used the quantity  $(1-\kappa)$  as a distance measure in a final hierarchical clustering, assigning the TFs to 10 clusters, to provide the cluster identities shown in **Figure 3C**.

## RNA Sequencing and Differential Expression Calling

1260 RNA-seq data sets were subjected to the same initial preprocessing and quality control steps as outlined above for the DNA samples, and then gene-level expression was quantified using kallisto v0.43 [72] on a version of the MG1655 (GenBank NC\_000913) genome with all ribosomal RNAs removed. Gene-level transcript per million (TPM) values from kallisto were used for all downstream analysis unless otherwise noted. To generate high-resolution occupancy plots, reads were instead aligned with bowtie2 as described above for DNA reads, and read occupancies quantified using the genomecov command of bedtools2 [73].

## TFBS Comparison

1270 Binding sites identified from IPOD-HR peaks (as described above in the “Feature calling” paragraph) were cross-referenced with known and predicted TFBSs using bedtools v2.17.0 [73]. “Known” sites comprise all binding sites contained in the RegulonDB release 9.4 BindingSiteSet.txt file [7]; “predicted” sites are identified by scanning the MG1655 (GenBank NC\_000913) genome with FIMO [74] using all *E. coli* position weight matrices from SwissRegulon [75] (as distributed by the MEME project); each PWM was applied separately, and all sites with a q-value less than 0.2 were retained. Default settings were used for FIMO, except that the background was a second-order Markov model based on the NC\_000913 genome, and the number of maximum stored scores was set to 10,000,000.

## Motif Identification

1280 Novel sequence motifs implied by IPOD-HR data were identified using an inference pipeline built off of FIRE [76]. Occupancy peaks and associated discrete threshold scores in the IPOD-HR traces were called using the CWT-based approach described above, using a score threshold of 4; each peak was assigned a discrete score corresponding to the average IPOD-HR occupancy score within that peak, rounding down. We then generated a background distribution of unbound sequences drawn from the portion of the genome not included in peaks, matching the length distribution of the peaks but with three times as many locations; all such background regions were assigned a score of 0 to distinguish them from the various thresholded peak regions.

1290 Motifs were called using FIRE with two separate variations: FIRE\_gapped (with parameters --kungapped=6 --gap=0-10 --jn\_t\_gapped=4 --minr=0.5), which searches for gapped motifs typical of prokaryotic transcription factor binding sites; and FIRE\_maxdeg (with parameters --jn\_t=8 --minr=1.5 --maxdeg=1.8), which searches for motifs while preserving information content above a specified threshold. We applied additional empirical filters to specifically enrich for peaks corresponding to binding sites: all peaks identified via FIRE

were required to have the motif significantly depleted from the background population ( $p < 0.01$ ). To assess the false discovery rate of our methods, we also generated 20 decoy peak sets by shuffling the locations of the real peaks observed in each condition, along with corresponding randomized unbound sets for each, and then applied identical peak calling procedures to each decoy set.

To avoid repeated reporting of very similar motifs which might be identified by our pipelines, we applied the matrix-clustering module of RSAT [77] (using recommended thresholds `-lth cor 0.7 -lth w 5 -lth Ncor 0.4`) to obtain non-redundant motif sets for downstream analysis. We compared all called motifs with previously known motifs from the SwissRegulon database using TOMTOM [34] with default parameters, requiring an E-value of 0.5 or lower for 'Identified' hits. For the identification of predicted regulons associated with each motif, we applied the FIMO program [74] to identify potential binding sites on the *E. coli* K12 genome, with a q-value threshold of 0.2; these were referred to as 'strict' motif hits. For the subset of predicted motifs that yielded no potential binding sites at this threshold, we instead report all locations that correspond to the FIMO score of the best single location found in the genome, referring to these as 'loose' motif hits. For the purposes of our analysis of the potential regulatory networks of novel motifs), we marked each transcriptional unit in *E. coli* as being regulated by a particular motif if and only if a predicted binding site for that motif was within 100 bp of the annotated transcription start site (in RegulonDB) for that transcriptional unit.

### In vitro pulldown of unidentified transcription factors

In order to identify the protein(s) binding to the *sdaC* promoter (as in **Fig. 4**), we first prepared biotinylated bait DNA by cloning a fragment of the *sdaC* promoter (running from positions 2927790 to 2927975 in the U00096.3 genome) into a pAZ3-based cloning vector [78], and then amplifying that region of the plasmid using a primer pair where one primer contained a 5' biotinylation. The resulting 486 bp fragment was treated with Exonuclease I (Affymetrix) according to the manufacturer's instructions to remove unreacted primer, and then purified using a Zymo Clean & Concentrate 25 kit.

The biotinylated bait DNA was then bound to equilibrated Dynabeads MyOne Streptavidin C1 beads (Invitrogen). Beads were equilibrated by washing three times with 1x B&W buffer (5 mM Tris Cl, pH 7.5; 0.5 mM EDTA; 1 M NaCl) and then resuspended in five volumes of 2x B&W buffer, using 42  $\mu$ L of the original resuspended bead solution per reaction. The equilibrated beads were combined with 8  $\mu$ g of biotinylated bait DNA plus an appropriate volume of water to yield a final 1x B&W solution, and incubated 15 minutes at room temperature with gentle rocking to allow for bait binding. The beads were then washed three times with 500  $\mu$ L of 1x B&W buffer, twice in 500  $\mu$ L of 1x BMg/THS buffer (5 mM HEPES, pH 7.5; 5 mM MgCl<sub>2</sub>; 50 mM KCl; 31 mM NaCl; 1x cComplete EDTA-free protease inhibitors (Roche)), once with 500  $\mu$ L of 1x BMg/THS/EP buffer (1x BMg/THS buffer supplemented with 20 mM EGTA (pH 8.0) and 10

1335  $\mu\text{g/mL}$  poly d(IC) (Sigma)). The beads were then resuspended in 200  $\mu\text{L}$  of BMg/THS/EP buffer and gently mixed by hand for one minute to complete equilibration.

1340 Cell extracts were prepared by growing to an  $\text{OD}_{600}$  of 0.2 in M9/RDM/glucose media (following the same procedures as those given for IPOD-HR experiments). Once reaching the target OD, the cells were chilled 10 minutes on ice, and then pelleted by spinning for 10 minutes at 5,500xg while at 4° C. Supernatant was removed, and the cells were flash-frozen in a dry ice/ethanol bath. Cells were then lysed by resuspending the frozen pellet resulting from 82 mL of culture in 160  $\mu\text{L}$  of B-PER II bacterial protein extraction reagent (Thermo Scientific). We then added 3.8 mL of 1x BMg/THS buffer and 0.8  $\mu\text{L}$  of ReadyLyse lysozyme solution (Lucigen), 40  $\mu\text{L}$  of 10 mg/mL RNase A, 20  $\mu\text{L}$  of  $\text{CaCl}_2$ , and 200  $\mu\text{L}$  of micrococcal nuclease (NEB; 2,000,000 gel units/mL). The lysis/digestion reaction was allowed to proceed for 30 minutes at room temperature, and then clarified by centrifugation at 30 minutes at 16,100x g held at 4° C. The reaction was halted by the addition of 444  $\mu\text{L}$  of 5 M NaCl, and then the entire volume applied to a 3 kDa MWCO spin filter (Amicon Ultra; Millipore) and centrifuged at (3,200 x g held at 4° C) until ~400  $\mu\text{L}$  of retentate remained. We then added 3.6 mL of BMg/THS (lacking NaCl and KCl, but containing 5 mM  $\text{CaCl}_2$ ) and filtered to 400  $\mu\text{L}$  of retentate. Retained liquid was then recovered, and diluted to a final volume of 4.0 mL with addition of salt-free BMg/THS + 5 mM  $\text{CaCl}_2$ . The retained lysate was then incubated 30 minutes at room temperature to permit further activity of micrococcal nuclease on remaining DNA in the sample, and then quenched with 168  $\mu\text{L}$  of 500 mM EGTA. The volume of the sample was reduced to approximately 1.6 mL by ultrafiltration as above, and further supplemented with 10  $\mu\text{g/mL}$  of poly d(IC) and 1 mM dithiothreitol.

1360 Probing of the lysates was then accomplished by combining the equilibrated bait-bead complexes (described above) with the lysates, and incubating 30 minutes with rocking at room temperature. The supernatant was then removed, and the beads washed twice with 200  $\mu\text{L}$  of BMg/THS/20 mM EGTA/10  $\mu\text{g/mL}$  poly d(IC), and once with 200  $\mu\text{L}$  of BMg/THS/20 mM EGTA. Proteins were then eluted from the beads through progressive washes of elution buffer (25 mM Tris HCl, pH 7.5) with 100 mM NaCl, 200 mM NaCl, 400 mM NaCl, and 1 M NaCl, with 50  $\mu\text{L}$  used for each elution.

1370 We successively probed the lysates described here with probes containing promoter sequences from *lexA*, *purR*, and finally, *sdaC* (each containing identical plasmid-derived flanking sequences). A ~25 kDa band of interest appeared in the 400 mM and 1 M NaCl *sdaC* eluates but not eluates from a parallel experiment performed under identical conditions with a segment of the *thiC* promoter; these bands were excised from a silver-stained gel. The 400 mM gel slice was then subjected to proteomic analysis at the University of Michigan Proteomics & Peptide Synthesis core facility. The gel slice was processed using a ProGest robot (DigiLab) to wash with 25 mM ammonium bicarbonate followed by acetonitrile, reduce with 10 mM dithiothreitol at 60° C followed by alkylation with 50 mM iodoacetamide at room temperature, digested with trypsin (Promega) at 37° C for 4 hours, and then quenched with formic acid. The digest was then analyzed by nano LC-MS/MS with a Waters NanoAcquity HPLC system interfaced to a ThermoFisher Q Exactive. Peptides were loaded on a trapping column and eluted over a 75  $\mu\text{m}$

1380 analytical column at 350 nL/min; both columns were packed with Jupiter Proteo resin  
(Phenomenex). The injection volume was 30  $\mu$ L. The mass spectrometer was operated in data-  
dependent mode, with the Orbitrap operating at 60,000 FWHM and 17,500 FWHM for MS and  
MS/MS respectively. The fifteen most abundant ions were selected for MS/MS. Data were  
1385 searched using a local copy of Mascot, and Mascot DAT files were parsed into the Scaffold  
software for validation, filtering and to create a non-redundant list per sample. Data were filtered  
using 90% protein and 95% peptide probability thresholds (Prophet scores) and requiring at  
least two unique peptides per protein). The resulting mass spectrometry analysis is given in  
**Table S2** after manual pruning by core staff of common contaminants (e.g. human keratin).

## Miller assay

1390 Cells containing the *lacZ* reporter controlled by *sdaC* promoter variants (see strain construction  
notes above) were grown overnight in M9 RDM media with 0.4% glucose. In the morning, cells  
were diluted 1:300 in fresh, prewarmed M9 RDM media with 0.4% glucose in 96 well plate. The  
plate was placed in a BioTek Synergy H1 plate reader measuring OD600 and grown until mid-  
exponential phase, around 6 doublings. Once the cells reached the target OD of around 0.2 (1  
1395 cm path length equivalent), 80uL of cells were placed in a new 96 well plate and mixed with 120  
uL of  $\beta$ -galactosidase assay mix (see below), avoiding the production of bubbles. The plate was  
loaded into the same Synergy H1 plate reader and incubated at 37° C, taking measurements  
every 2 minutes for 1 hour. Our procedure, assay, and analysis for the Miller assay are adapted  
from [79].

1400

Reagents:

- Z-buffer: 60mM Na<sub>2</sub>HPO<sub>4</sub>, 40mM NaH<sub>2</sub>PO<sub>4</sub> , 10mM KCl, 1mM MgSO<sub>4</sub>
- $\beta$ -mercaptoethanol solution: 2.7 $\mu$ L/mL  $\beta$ -mercaptoethanol in Z-Buffer
- ONPG solution: 4mg/mL ONPG in Z-Buffer
- 1405 • Lysozyme solution: 10mg/mL lysozyme in 10mM Tris-HCl, pH=8.0

$\beta$ -galactosidase assay mix (100 reactions):

- 8mL  $\beta$ -me solution
- 3mL ONPG solution
- 1410 • 800 $\mu$ L PopCulture Reagent (Sigma Aldrich)
- 200 $\mu$ L Lysozyme solution

1415 We then calculated the enzymatic activity in each well first by subtracting 1.7 times the OD550  
value at each timepoint from the OD420 value (to yield the amount of enzymatic product after  
correcting for cell debris), and then fitting a LOESS smoothing curve to the resulting values and  
identifying the point of maximal slope; that slope (which is a rate of increase in product vs. time)  
is taken as the enzymatic activity. The background activity of MG1655 *lacZ::cmI* cells measured  
at the same time was then subtracted from each data point. The activities were then divided by  
the OD600 of the corresponding cells used in each assay to account for the differing amounts of

1420 biological starting material, to yield final OD-normalized Miller units. The experiments were performed in technical duplicate on each of four different days.

The resulting normalized Miller values were then analyzed using a Bayesian mixed-effects model to identify the relative promoter activities in our eight strains of interest. We assumed that  
1425 the normalized Miller values followed the form

$$M_{\text{cent}} \sim t(\alpha_{\text{date}} + \beta_{\text{strain}} + \gamma_{\text{date:strain}}, \sigma, \nu)$$

Where  $\alpha$  and  $\beta$  are fixed effects representing the effects of experimental date and of the *yieP*/promoter  
1430 genotypes, respectively; the  $\gamma$  is a random effects term with levels for each date/strain combination, and  $\sigma$  and  $\nu$  are the standard deviation and degrees-of-freedom parameters of the  $t$  distributed residual noise.  $M_{\text{cent}}$  indicates centered Miller units where the global mean of all measurements was subtracted from each value (the fitted coefficients were then de-centered prior to plotting). The model was fitted using the `brms` [80] module of R; using a `normal(0,1000)`  
1435 prior on each of the fixed effects, a `t(0,500,10)` prior on the standard deviation parameter, and defaults for all other parameters (the mildly informative priors used here were based on the behavior of wild type MG1655 cells induced by IPTG in our assay). Model convergence was assessed using the `Rhat` metric and manual inspection of the posterior predictive distribution.

## Data Availability

1440 The raw and processed sequencing data used in this study have been deposited in the Gene Expression Omnibus.

## Acknowledgments

1445 This work was supported by NIH grants R00-GM097033 and R35-GM128637 (to PLF) and R01-AI077562 (to ST). We are grateful to Dr. Alison Hottes for technical assistance and suggestions on the original IPOD method, and to Ms. Christine Ziegler for optimization of the Miller assay as used in Fig. 4.

## Author Contributions

1450 Conceptualization, S.T.; Methodology, P.L.F. and S.T.; Investigation, P.L.F., T.J.G., and H.A.; Data Analysis and Curation, P.L.F. and S.T.; Writing -- Original Draft, P.L.F. and S.T.; Writing -- Review & Editing, P.L.F., H.A., and S.T.; Funding Acquisition, P.L.F. and S.T.

1455

## Declaration of Interests

The authors have no competing interests.

## Supplementary Text

### 1460 **Supplementary Text S1: Effects of RNA polymerase on large-scale protein occupancy**

In the IPOD-HR method, we address the contribution of RNA polymerase occupancy to the overall protein occupancy signal through two steps: first, immediately prior to crosslinking, cells are treated with rifampin for 10 minutes. We have calibrated the rifampin treatment to allow  
1465 sufficient time for in-progress transcripts to finish while minimizing perturbation of cellular physiology (building on data from [81], as well as direct calculation of the required time based on the elongation rate of RNA polymerase and lengths of *E. coli* transcripts). As rifampin inhibits promoter clearance but not the transcriptional initiation nor completion of already-elongating transcripts [82], the result will thus be to cause an accumulation of RNA polymerase at active  
1470 promoters, while clearing the majority of polymerase occupancy from gene bodies, and thus substantially simplifying the identification of RNA polymerase occupancy. In addition, all IPOD-HR experiments described here were performed in parallel with RNA polymerase ChIP-seq experiments under the same conditions, permitting calibrated subtraction of RNA polymerase occupancy from active promoters to reveal changes in regulatory protein occupancy (as  
1475 schematized in **Figure 1B-C**). However, the fact that transcriptional inhibition is known to affect nucleoid condensation [83–86] prompted us to directly inspect the effects of rifampin on genome-wide protein binding, with a particular emphasis on the effects on EPOD formation and transcription factor binding.

1480 To illustrate the effects of rifampin treatment on regions of extremely high or low RNA polymerase occupancy, we performed IPOD experiments under our baseline growth condition (WT cells undergoing exponential growth in M9/RDM/glu medium) following the same procedure as used for all other samples in the present study, but omitting the rifampin treatment (*n.b.* the data sets of [10] were obtained under a slightly different condition, during exponential growth in  
1485 LB medium). An overall analysis of the resulting EPOD calls (**Fig. S5**) demonstrates that the -RIF EPOD set arising from our methods show good correlations with both the heEPOD and tsEPOD calls from [10], whereas the +RIF EPOD set from our method (used throughout the rest of text) shows a much stronger correlation with the Vora tsEPOD set and a weaker correlation with heEPODs. It is also important to note that the fraction of locations from the Vora tsEPOD  
1490 set that is contained within our relaxed +RIF EPOD calls (0.89) is in line with the equivalent overlaps between the EPOD sets observed across different conditions in our main data sets (upper triangle of **Fig. 6D**), further indicating that the EPODs identified via IPOD-HR closely resemble the original Vora tsEPODs.

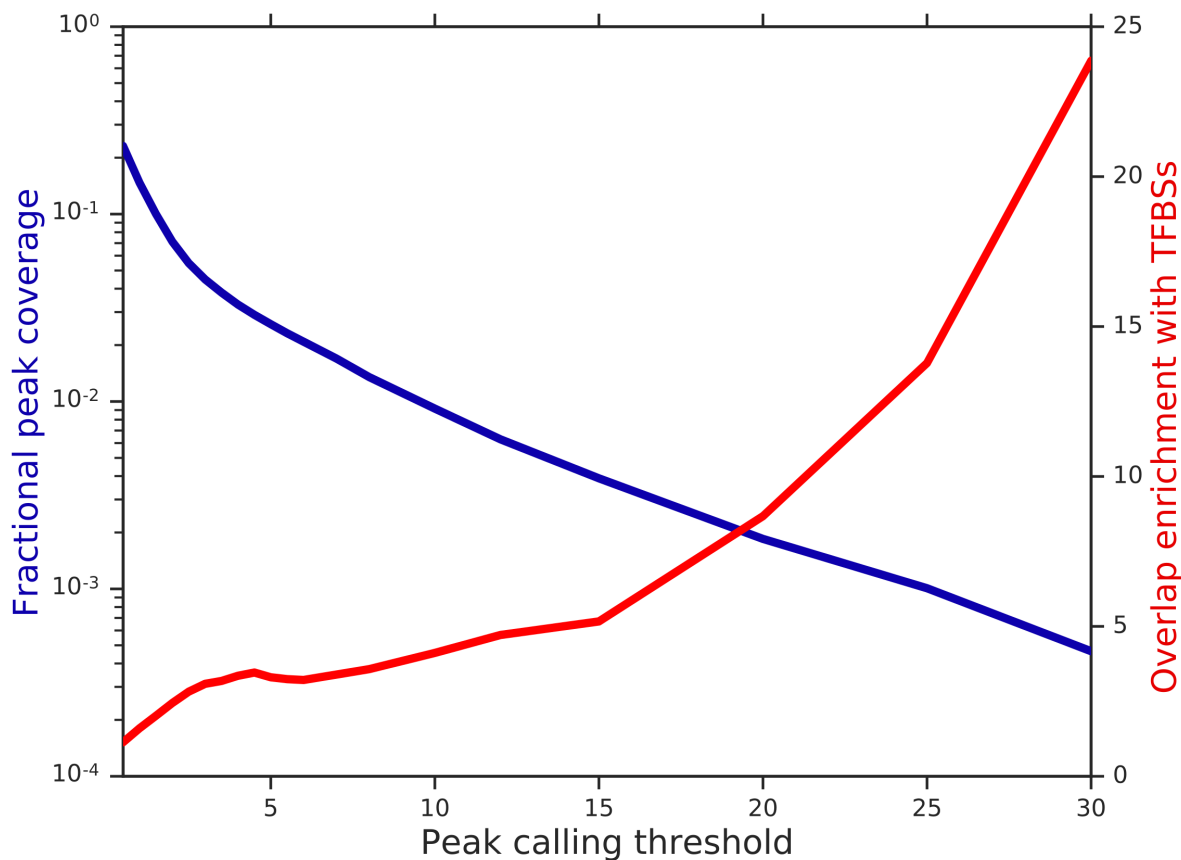
1495 To obtain a more detailed picture of the effects of rifampin on protein occupancy in our assays, we show an example of a highly expressed EPOD (heEPOD) from the original IPOD data sets in **Figure S6**. In the original IPOD data set [10], strong protein occupancy was noted throughout the cluster of ribosomal protein operons running from *rplQ* to *rpsJ*. Here, we see from the rifampin-omitted (-RIF) samples that the protein occupancy profile in this region is dominated by  
1500 RNA polymerase occupancy, closely matching the bounds of the originally called heEPOD. On

the other hand, in the rifampin-treated samples (+RIF), the vast majority of occupancy in this region is lost, with peaks only apparent at a few points within the region of interest (likely corresponding to highly active promoters). After subtraction of the scaled RNA polymerase occupancy to yield the IPOD-HR signal, the only prominent peak remaining in the region is in the *gspA-gspC* intergenic region, which has been demonstrated to be repressed by H-NS binding (although the precise binding location was previously unknown [87]).

The occupancy observed in the ribosomal protein operon cluster described above contrasts strongly with that seen in the transcriptionally silent EPODs (tsEPODs) found in [10]. In the region of the tsEPOD shown in **Figure S7**, for example, we observe that in the -RIF samples, there is continuous protein occupancy but essentially no RNA polymerase occupancy throughout the large tsEPOD that was originally observed to span the *waaQGPSBOJYZU* operon, whereas both strong IPOD occupancy and strong RNA polymerase occupancy are apparent on a nearby heEPOD covering the *rpmBG* operon. Treatment with rifampin does not substantially alter the high level of overall protein occupancy throughout the *waa* region, whereas it restricts occupancy near *rpmBG* to active promoters only. As a result, in the ChIP-subtract IPOD-HR signal, strong occupancy remains throughout the *waaQGPSBOJYZU* operon, resulting in an EPOD call nearly identical to the original tsEPOD in that region from [10]. One feature of the +RIF samples that requires consideration is the fact that several RNA polymerase occupancy peaks appear in regions such as tsEPODs where no comparable occupancy is apparent in -RIF samples. We attribute these additional peaks to the fact that during rifampin treatments, concentrations of free RNA polymerase will rise substantially due to the immobilization of polymerase at transcription start sites; thus, occupancy at normally weak promoters through the chromosome will increase. We find, however, that the ChIP-subtraction step of our IPOD-HR data processing pipeline accurately removes RNA polymerase occupancy at both normally-active promoters and those showing RNA polymerase binding only in the presence of rifampin treatment (as seen by the well-calibrated removal of RNA polymerase occupancy in the +RIF tracks of **Figures S6-S7**, for example). Overall, we find that even in the +RIF samples, RNA polymerase occupancy remains very well correlated with transcript levels (**Figure 3E**), can be cleanly subtracted to yield condition-appropriate changes in transcription factor occupancy (**Figure 1C**); furthermore, brief rifampin treatment does not appear to substantively alter large-scale protein occupancy other than that directly attributable to RNA polymerase binding (**Figures S6 vs S7**). Given that rifampin treatment permits cleaner subtraction of RNA polymerase occupancy, while not perturbing either the local or large-scale protein binding patterns that are the subject of our interest, we make use of it throughout the IPOD-HR data sets shown in the present work.



## Supplementary Figures



1540

**Figure S1: Effect of peak calling threshold on coverage and enrichment of known**

**transcription factor binding sites (TFBSs).** Data are shown for the wild type cells in the rich defined medium condition. Shown is the fraction of the entire genome contained in peak calls (left vertical axis, blue line) or the enrichment of TFBSs overlapping those peak calls relative to that expected by chance (right vertical axis, red line). Overlaps at all shown thresholds were statistically significant ( $p < 0.01$ , permutation test in each case).

1545

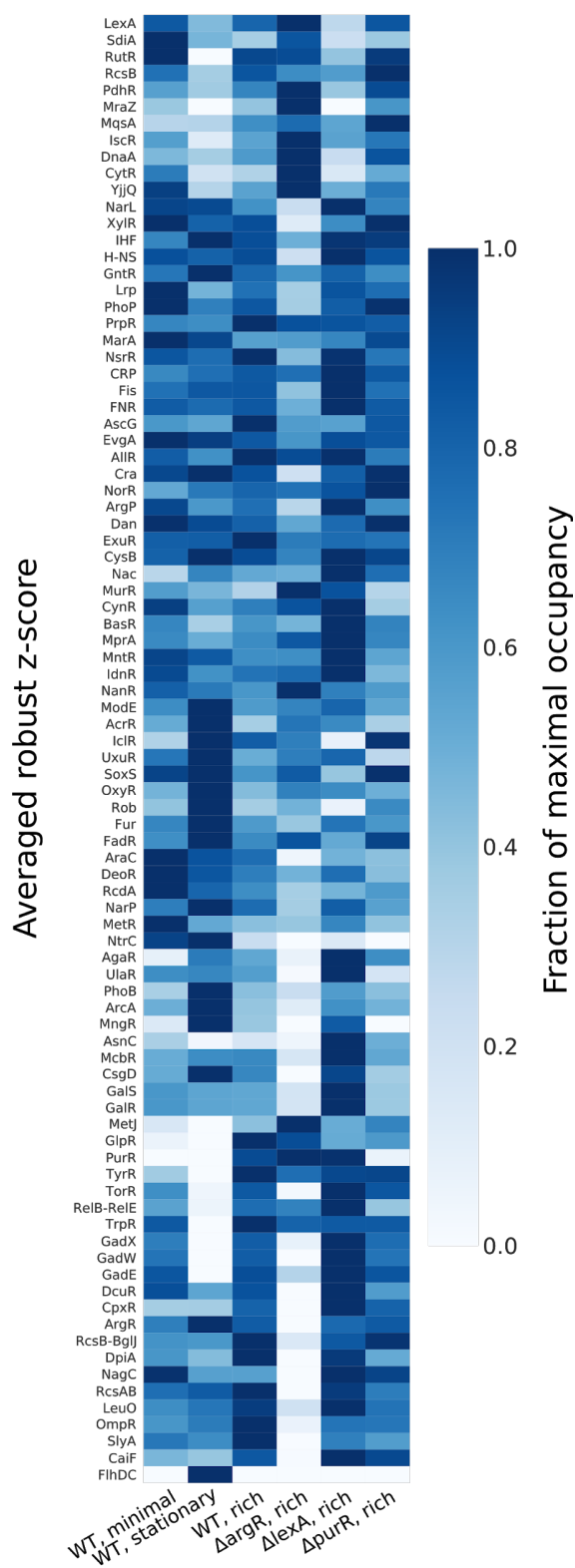
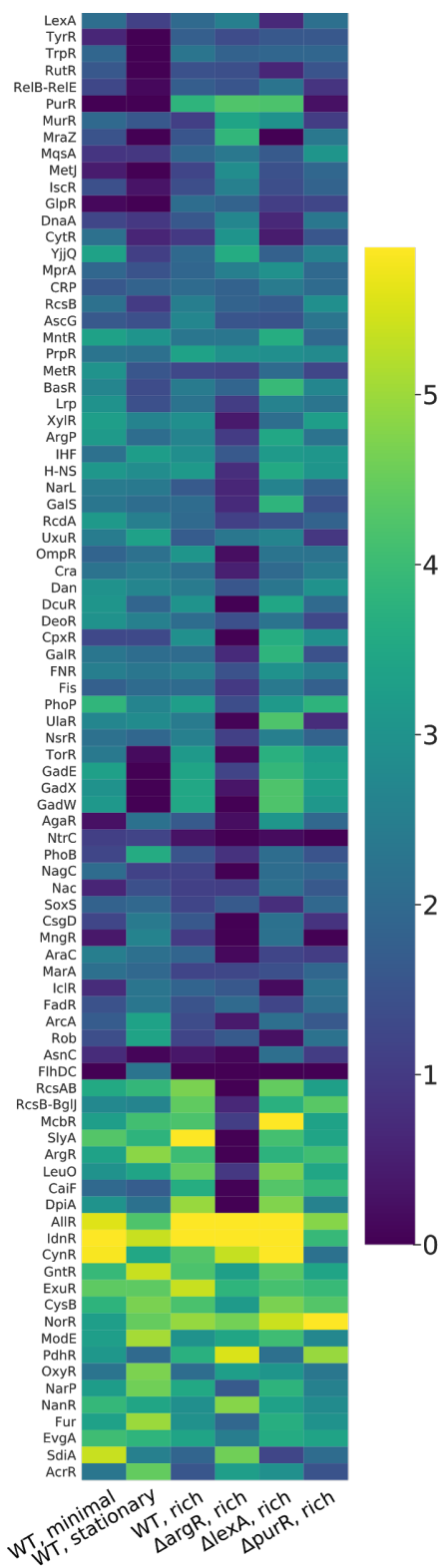
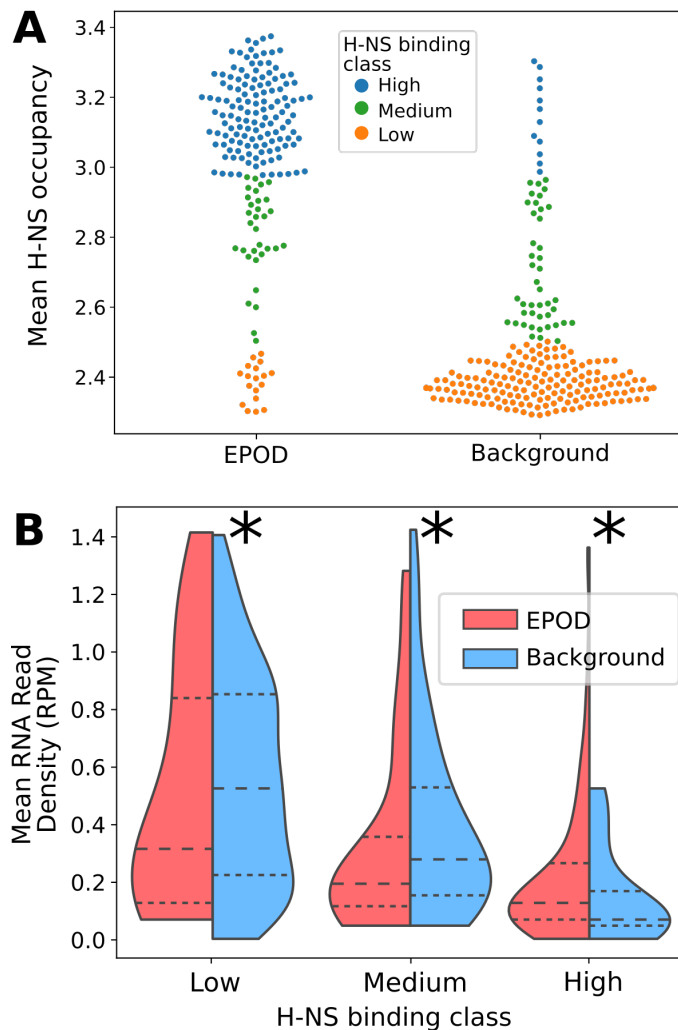


**Figure S2: Average occupancies for transcription factors with known/characterized binding sites.**

1555 (A) Shown for each transcription factor (row) is the geometric mean of site-level occupancies for all detectable sites for that TF under that condition. “Detectable sites” refer to RegulonDB-annotated sites which had a robust z-score of at least 3 under at least one condition; factors with fewer than 3 detectable sites were excluded. The values within a single site, for a single condition, are summarized by the maximum occupancy within that site, reflecting the peak of the observed binding signal. The TFs are ordered based on a consensus clustering approach as applied for **Fig. 3B** of the main text. Raw data on the underlying site-level occupancies are given in **Supplementary Data S7**. (B) As in **A**, subsequently scaling each row by its maximum value so the highest-occupancy condition for each TF receives a score of 1.0.

1560



1565 **Figure S3: Interplay of H-NS occupancy, EPOD locations, and transcription. (A)** Mean  
levels of H-NS binding (data from [42]) for all EPODs called in the WT rich media condition;  
each point shows either an EPOD or a single contiguous non-EPOD region. Each point is  
colored by its classification into high, medium, or low H-NS binding using a Gaussian mixture  
model with three groups, after removal of outliers using the local outlier factor [88] as  
1570 implemented in the python scikit-learn module [89], using 25 neighbors and default settings for  
other parameters. **(B)** Distributions of mean RNA read density stratified by the H-NS binding  
categories shown in panel **A**, with each case divided by EPOD status. The median of each  
group is shown by a dashed line, and the 25th and 75th quartiles by dotted lines. “\*” indicates a  
significant difference between the EPOD vs. background groups ( $p < 0.05$ , Mann-Whitney U  
1575 test).

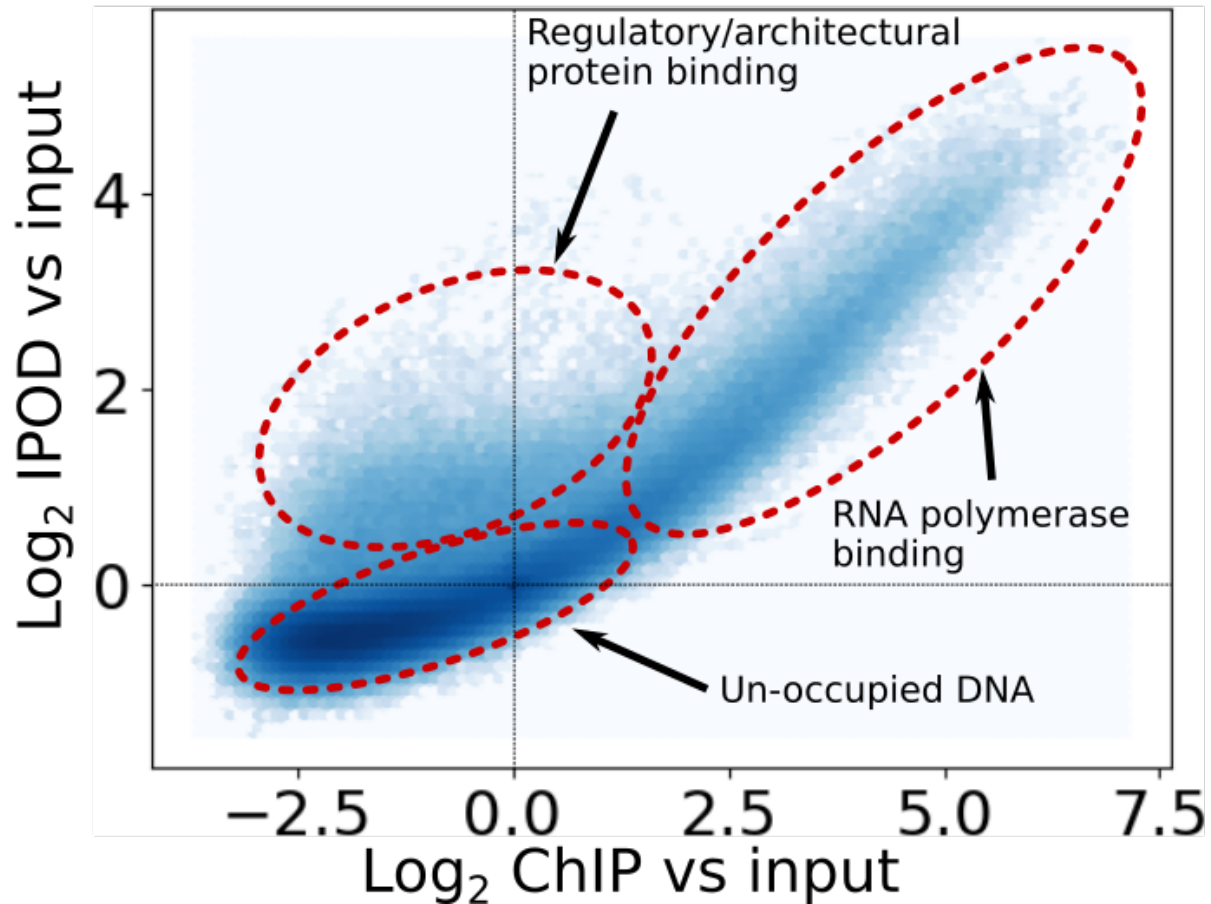
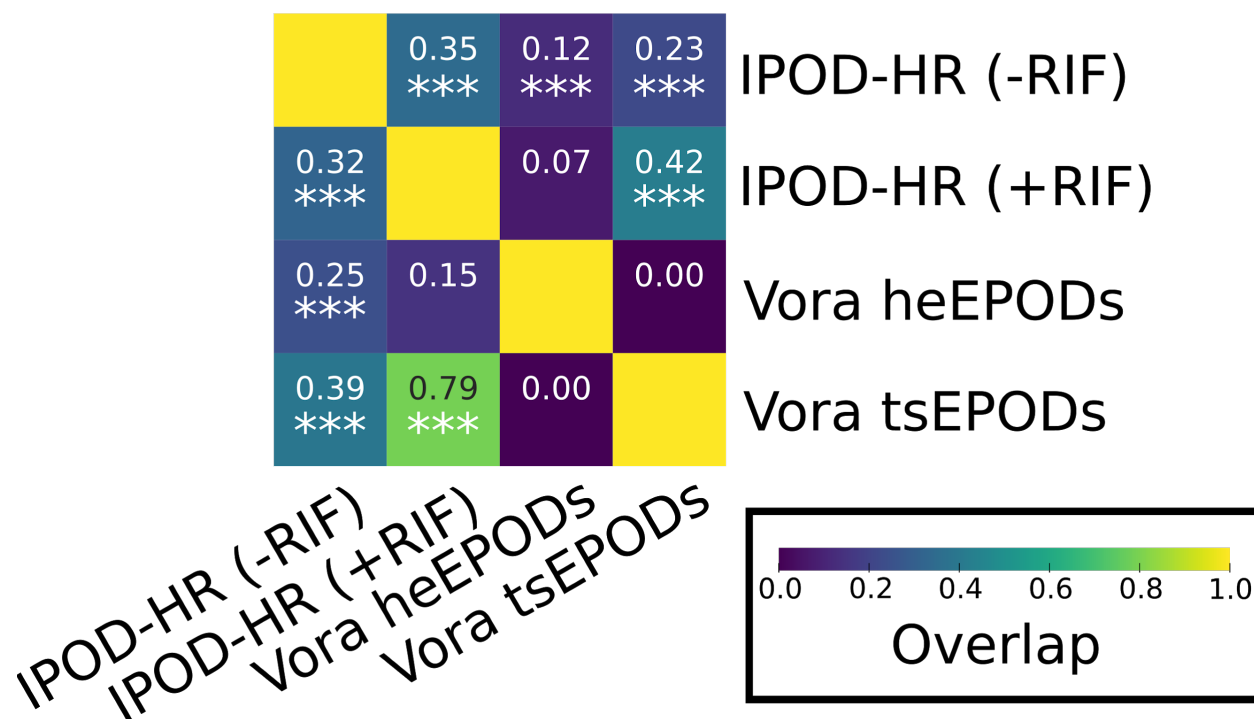


**Figure S4: Identification of RNA polymerase vs. non-RNA polymerase protein occupancy.**

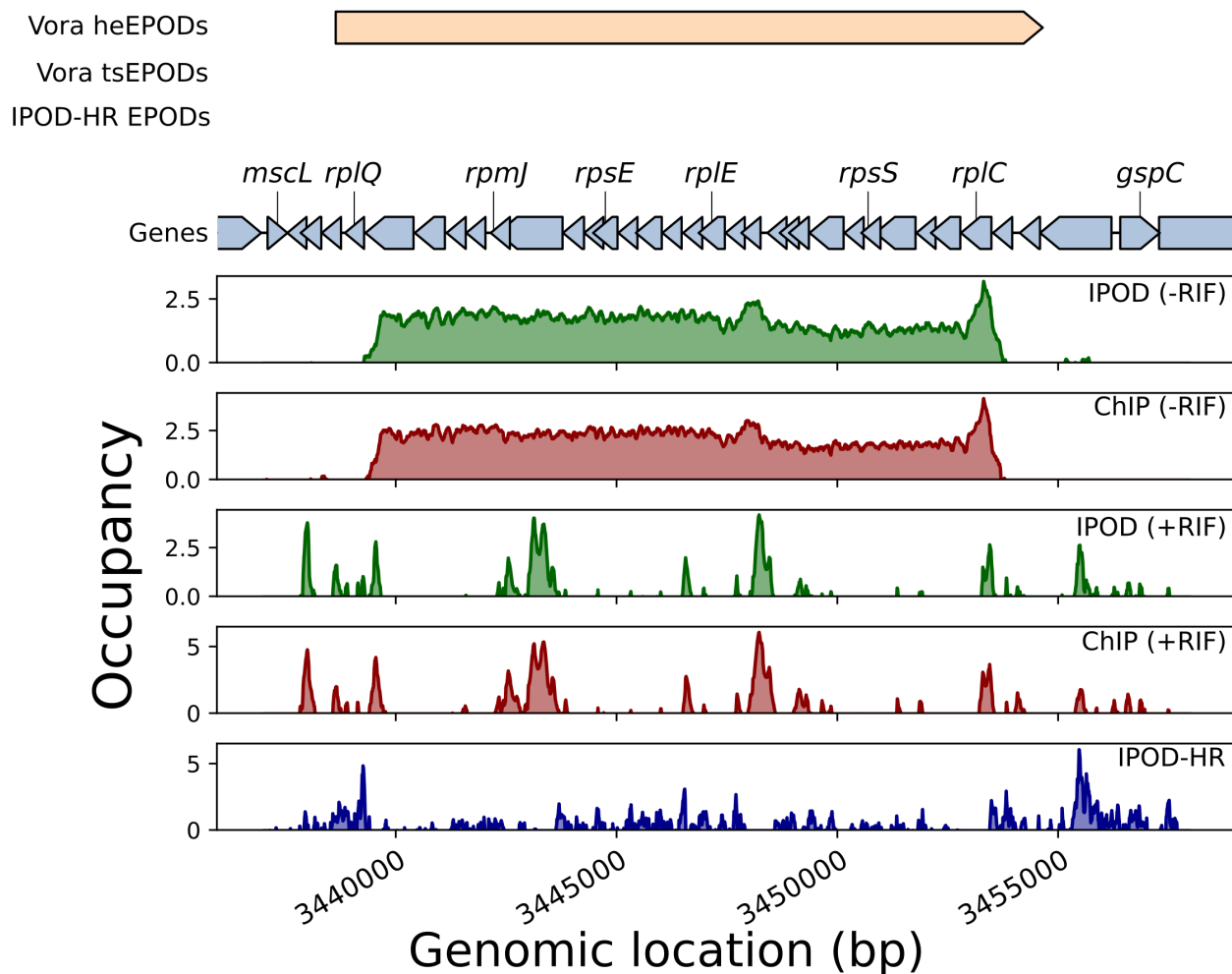
1580

Shown is a density plot of the  $\log_2(\text{IPOD}/\text{Input})$  signal vs.  $\log_2(\text{RNA polymerase ChIP}/\text{Input})$  signal, demonstrating the presence of three subpopulations of genomic positions: unbound positions (without enrichment using either protein occupancy profiling method), RNA polymerase occupancy (part of a highly correlated region of high IPOD occupancy and high RNA polymerase occupancy), and occupancy with other proteins (which shows high IPOD occupancy but low RNA polymerase occupancy). Note that there is no corresponding population of high RNA polymerase occupancy but low IPOD occupancy; rather, the RNA polymerase-bound regions are a subset of the regions detected by IPOD. Color intensity scales linearly with bin occupancy.

1585

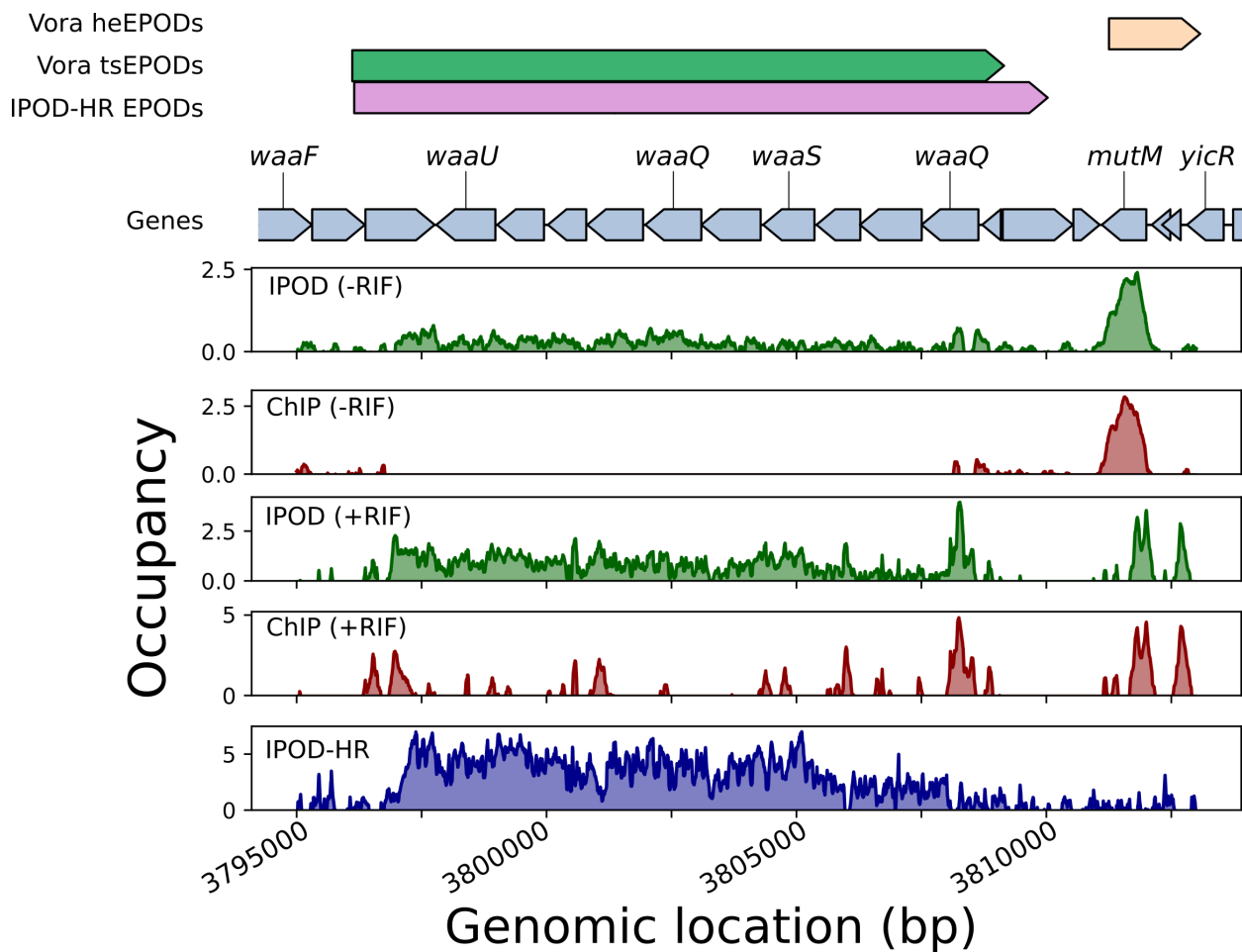


1590 **Figure S5: Overlaps of EPOD sets resulting from different calling methods.** Shown in the  
 1595 heatmap are the fraction of EPODs from the EPOD set defined by the row label that overlap the  
 EPOD set defined by the column label. Asterisks reflect p-values arising from a Monte Carlo  
 permutation test (1000 random circular permutations of the EPOD locations; \* p<0.05, \*\*  
 p<0.01, \*\*\* p<0.001). p-values for the overlaps between the +RIF IPOD-HR EPOD set and the  
 Vora heEPODs were >0.8 for both directions of comparisons; a full list of values is given in  
**Table S4.**



1600

**Figure S6: Effects of rifampin treatment on protein occupancy of a highly transcribed region.** Shown are occupancy signals for interphase-extracted, RNA polymerase ChIP, and ChIP-subtracted IPOD occupancy (IPOD-HR) samples in the vicinity of a large cluster of ribosomal protein genes (running from *rplQ* to *rpsJ*). Signals are log<sub>2</sub> extracted:input ratios (for IPOD and ChIP samples), or ChIP-subtracted robust z scores (IPOD-HR).



1605

**Figure S7: Effects of rifampin treatment on protein occupancy of a transcriptionally silent region.** Shown are occupancy signals for interphase-extracted, RNA polymerase ChIP, and CHIP-subtracted IPOD occupancy (IPOD-HR) samples in the vicinity of the *waaQGPSBOJYZU* operon, which was identified as a strong tsEPOD in [10]. Signals are log<sub>2</sub> extracted:input ratios (for IPOD and ChIP samples), or ChIP-subtracted robust z scores (IPOD-HR).

1610



## Supplementary Tables and Data Files

1615 **Table S1:** Comparisons of the distributions of robust z-scores (without log scaling) observed on  
different genomic regions in the “WT,rich” condition; see also cumulative distributions of the  
log<sub>10</sub>p statistic in **Fig. 2E**. The higher means and rightward skews of all other data sets relative  
to the “Coding, No TF” portion indicates that the portions of the genome with higher IPOD-HR  
robust z-scores are associated with noncoding regions and annotated TFBSs. The “vs. Coding  
1620 No TF” column gives the p-value for a permutation test comparing the mean z-scores in the  
indicated genomic region with those in the “Coding, No TF” region; the permutation test was  
conducted using 200 random rotations of the data values relative to the feature coordinates,  
ensuring that the correlation structures of both data and features were conserved.

Genomic Region	Mean	Standard deviation	Skew	vs. Coding No TF
Noncoding, No TF	0.80	2.08	0.38	<0.005
Noncoding, TF site	1.06	2.31	0.65	<0.005
Coding, No TF	0.17	1.26	-0.03	--
Coding, TF Site	0.34	1.69	0.20	0.075
(Standard normal)	0.00	1.00	0.00	--

1625

**Table S2:** Mass spectrometry identified peptide counts showing abundances of proteins pulled down by biotinylated bait DNA from the *sdaC* promoter region, after pruning of likely contaminants (see Methods for details).

Identified protein	Accession Number	Molecular Weight	Total Spectrum Count
UlaR	tr C3SFV2 C3SFV2_EC OLX	28 kDa	16
YieP	tr E2QHU3 E2QHU3_EC OLX	26 kDa	9
RpsC	tr C3SQX2 C3SQX2_EC OLX	26 kDa	7

RpoC	tr C3SIA2 C3SIA2_ECO LX	155 kDa	11
RpoB	tr E2QJ13 E2QJ13_ECO LX	151 kDa	7
RuvA	tr C3T5R2 C3T5R2_EC OLX	22 kDa	10
FliA	tr C3SDE6 C3SDE6_EC OLX	28 kDa	6
RpoA	tr C3SR67 C3SR67_EC OLX	37 kDa	7
RpsD	tr C3SR62 C3SR62_EC OLX	23 kDa	3
RdgC	tr E2QGD8 E2QGD8_EC OLX	34 kDa	3
UvrA	tr C3SHF7 C3SHF7_EC OLX	104 kDa	5
CysB	tr C3TC57 C3TC57_EC OLX	36 kDa	5
FabR	tr E2QIZ8 E2QIZ8_ECO LX	24 kDa	4
GroL	tr Q548M1 Q548M1_EC OLX	57 kDa	3
IhfB	tr Q14F22 Q14F22_ECO LX	11 kDa	4
RplC	tr C3SQU2 C3SQU2_EC OLX	22 kDa	2
AccB	tr C3SRL7 C3SRL7_EC OLX	17 kDa	4
AmiA	tr E2QPR8 E2QPR8_EC OLX	31 kDa	3
IhfA	tr Q14F23 Q14F23_ECO LX	11 kDa	2
Ppx	tr C3T027 C3T027_ECO LX	58 kDa	2
RplB	tr C3SQV7 C3SQV7_EC OLX	30 kDa	2
RpoE	tr Q0P6M2 Q0P6M2_EC OLX	22 kDa	2
FabZ	tr C3TPH7 C3TPH7_EC OLX	17 kDa	3
PolA	tr E2QI51 E2QI51_ECOL	103 kDa	2

	X		
TufB	tr E2QFJ4 E2QFJ4_ECO LX (+1)	43 kDa	2

1630 **Table S3:** Summary of EPOD characteristics across experimental conditions. The “Median  
 difference” column refers to the difference in median robust Z-scores between EPODs and all  
 other sites in the genome, with positive values indicating higher levels within EPODs. P-values  
 for a significant difference are obtained using a resampling test, with 1000 random circular  
 1635 permutations of the EPOD locations on the genome (thus preserving the correlation structure of  
 genomic features); q-values are obtained by correction of the p-values using the Benjamini-  
 Hochberg method [90]. All sequence features were subjected to a 500 bp rolling mean prior to  
 overlap calculation.

Feature	Median difference	p value	q value	Reference
Transcriptional propensity	-1.009	0.001	0.001	[36]
Supercoiling density	-0.256	0.487	0.487	[91]
Normalized Tn5 integration density	4.605	0.001	0.001	[36]
Fis binding	-1.060	0.001	0.001	[42]
H-NS binding	12.068	0.001	0.001	[42]
HU binding	-0.289	0.042	0.048	[92]
LRP binding	0.462	0.091	0.097	[26]
SeqA binding	-0.255	0.003	0.004	[93]
Dam sites	-0.674	0.001	0.001	Sequence analysis
AT content	1.855	0.001	0.001	Sequence analysis
RNA	-0.682	0.001	0.001	Present study
MGW	-0.084	0.001	0.001	Calculated using DNAsapeR [94]
HelT	0.071	0.001	0.001	
ProT	-0.169	0.001	0.001	
Roll	-0.086	0.001	0.001	

1640

- 1645 **Table S4:** P-values arising from the statistical tests shown in **Figure 3C** (calculated using iPAGE software), and in **Figure S4** (arising from permutation tests in which the genomic coordinates of one EPOD set were rotated in unison relative to the other, to preserve the internal correlation structures of each group).
- 1650 **Table S5:** List of IPOD-HR experiments performed over the course of the study, including concise names used to refer to each experiment in the remainder of the text. (included as a separate file). Note that “Aligned reads” refers specifically to the number of concordant, uniquely aligned read pairs arising from a given sample, or the number of pseudoaligned reads in the case of an RNA sample.
- 1655 **Supplementary Data S1:** Bedgraph files showing the processed occupancy traces for the biological conditions considered in this study, corresponding to the plotted data.
- Supplementary Data S2:** GFF files containing the locations of all peak calls (with cutoffs indicated in the “score” field; see Methods for details) obtained from our IPOD-HR occupancy profiles through all conditions in the present study. The value in the ‘score’ column corresponds to the peak calling threshold in use. Note that the ‘strand’ and ‘frame’ fields convey no useful information.
- 1660
- Supplementary Data S3:** MEME-formatted file containing the complete set of redundancy-pruned motifs discovered across all conditions in the present study.
- 1665 **Supplementary Data S4:** GFF file giving the FIMO hits on the *E. coli* MG1655 genome for all newly inferred motifs described here. For factors that gave hits using our standard criterion (FIMO q-value <0.2), we flag hits as “Nucleotide motif (strict)”; for motifs that gave no hits according to this criterion, we instead report all locations that correspond to the FIMO score of the best single location found in the genome, flagged as “Nucleotide motif (loose)”.
- 1670 **Supplementary Data S5:** Table showing the GO terms that are enriched in the potential regulon of each newly inferred regulatory motif. The tab-separated table gives the motif name, GO term, and p-value (obtained from iPAGE ) for each inferred regulatory connection.
- Supplementary Data S6:** GFF file containing the locations of all EPODs called on our IPOD-HR occupancy profiles (see Methods for details). Note that the ‘score’, ‘strand’, and ‘frame’ fields convey no useful information.
- 1675
- Supplementary Data S7:** Table showing the occupancy at each detectable TFBS used in the analysis of **Fig. 3** and associated supplemental figures.
- Supplementary Data S8:** Table showing the Jaccard index between each of the newly inferred motifs, with all TFs that have characterized regulons in RegulonDB. Jaccard indices were calculated at the gene level (using gene names as individual items), using the definitions of regulated genes used elsewhere in the present paper for the newly inferred motifs, and the network\_tf\_gene.txt entries from RegulonDB (release 10.8). Motif indices match those in Supplementary Data S3 for members of the redundancy-pruned set.
- 1680

## References

- 1685
1. Browning DF, Butala M, Busby SJW. Bacterial Transcription Factors: Regulation by Pick “N” Mix. *J Mol Biol.* 2019. doi:10.1016/j.jmb.2019.04.011
  2. Lee DJ, Minchin SD, Busby SJW. Activating transcription in bacteria. *Annu Rev Microbiol.* 2012;66: 125–152.
- 1690
3. Gruber TM, Gross CA. Multiple sigma subunits and the partitioning of bacterial transcription space. *Annu Rev Microbiol.* 2003;57: 441–466.
  4. Murakami KS, Darst SA. Bacterial RNA polymerases: the whole story. *Curr Opin Struct Biol.* 2003;13: 31–39.
- 1695
5. Shen BA, Landick R. Transcription of Bacterial Chromatin. *J Mol Biol.* 2019. doi:10.1016/j.jmb.2019.05.041
- 1700
6. Ishihama A, Shimada T, Yamazaki Y. Transcription profile of *Escherichia coli*: genomic SELEX search for regulatory targets of transcription factors. *Nucleic Acids Res.* 2016;44: 2058–2074.
  7. Gama-Castro S, Salgado H, Santos-Zavaleta A, Ledezma-Tejeida D, Muñiz-Rascado L, García-Sotelo JS, et al. RegulonDB version 9.0: high-level integration of gene regulation, coexpression, motif clustering and beyond. *Nucleic Acids Res.* 2016;44: D133–43.
  8. Larsen SJ, Röttger R, Schmidt HHHW, Baumbach J. *E. coli* gene regulatory networks are inconsistent with gene expression data. *Nucleic Acids Res.* 2019;47: 85–92.
- 1705
9. Mejía-Almonte C, Busby SJW, Wade JT, van Helden J, Arkin AP, Stormo GD, et al. Redefining fundamental concepts of transcription initiation in bacteria. *Nat Rev Genet.* 2020. doi:10.1038/s41576-020-0254-8
- 1710
10. Vora T, Hottes AK, Tavazoie S. Protein occupancy landscape of a bacterial genome. *Mol Cell.* 2009;35: 247–253.
  11. Giresi PG, Kim J, McDaniel RM, Iyer VR, Lieb JD. FAIRE (Formaldehyde-Assisted Isolation of Regulatory Elements) isolates active regulatory elements from human chromatin. *Genome Res.* 2007;17: 877–885.
  12. Meng LM, Nygaard P. Identification of hypoxanthine and guanine as the co-repressors for the purine regulon genes of *Escherichia coli*. *Mol Microbiol.* 1990;4: 2187–2192.
- 1715
13. Cho B-K, Federowicz SA, Embree M, Park Y-S, Kim D, Palsson BØ. The PurR regulon in *Escherichia coli* K-12 MG1655. *Nucleic Acids Res.* 2011;39: 6456–6464.
  14. Tian G, Lim D, Carey J, Maas WK. Binding of the arginine repressor of *Escherichia coli* K12 to its operator sites. *J Mol Biol.* 1992;226: 387–397.
  15. Charlier D, Roovers M, Van Vliet F, Boyen A, Cunin R, Nakamura Y, et al. Arginine regulon of *Escherichia coli* K-12. A study of repressor-operator interactions and of in vitro binding

- 1720            affinities versus in vivo repression. *J Mol Biol.* 1992;226: 367–386.
16. Stragier P, Danos O, Patte JC. Regulation of diaminopimelate decarboxylase synthesis in *Escherichia coli*. II. Nucleotide sequence of the *lysA* gene and its regulatory region. *J Mol Biol.* 1983;168: 321–331.
17. Van Duyne GD, Ghosh G, Maas WK, Sigler PB. Structure of the oligomerization and L-arginine binding domain of the arginine repressor of *Escherichia coli*. *J Mol Biol.* 1996;256: 377–391.
- 1725            18. Rolfes RJ, Zalkin H. Purification of the *Escherichia coli* purine regulon repressor and identification of corepressors. *J Bacteriol.* 1990;172: 5637–5642.
19. Shimada T, Hirao K, Kori A, Yamamoto K, Ishihama A. RutR is the uracil/thymine-sensing master regulator of a set of genes for synthesis and degradation of pyrimidines. *Mol Microbiol.* 2007;66: 744–757.
- 1730            20. Pedersen H, Sogaard-Andersen L, Holst B, Valentin-Hansen P. Heterologous cooperativity in *Escherichia coli*. The CytR repressor both contacts DNA and the cAMP receptor protein when binding to the *deoP2* promoter. *J Biol Chem.* 1991;266: 17804–17808.
- 1735            21. Gerlach P, Sogaard-Andersen L, Pedersen H, Martinussen J, Valentin-Hansen P, Bremer E. The cyclic AMP (cAMP)-cAMP receptor protein complex functions both as an activator and as a corepressor at the *tsx-p2* promoter of *Escherichia coli* K-12. *J Bacteriol.* 1991;173: 5419–5430.
22. Gunsalus RP, Park SJ. Aerobic-anaerobic gene regulation in *Escherichia coli*: control by the ArcAB and Fnr regulons. *Res Microbiol.* 1994;145: 437–450.
- 1740            23. Iuchi S, Lin EC. Adaptation of *Escherichia coli* to redox environments by gene expression. *Mol Microbiol.* 1993;9: 9–15.
24. Solomon MJ, Varshavsky A. Formaldehyde-mediated DNA-protein crosslinking: a probe for in vivo chromatin structures. *Proc Natl Acad Sci U S A.* 1985;82: 6470–6474.
- 1745            25. McClure WR, Cech CL. On the mechanism of rifampicin inhibition of RNA synthesis. *J Biol Chem.* 1978;253: 8949–8956.
26. Kroner GM, Wolfe MB, Freddolino PL. *Escherichia coli* Lrp regulates one-third of the genome via direct, cooperative, and indirect routes. *J Bacteriol.* 2018. doi:10.1128/JB.00411-18
- 1750            27. Pique-Regi R, Degner JF, Pai AA, Gaffney DJ, Gilad Y, Pritchard JK. Accurate inference of transcription factor binding from DNA sequence and chromatin accessibility data. *Genome Res.* 2011;21: 447–455.
28. Shimada T, Ogasawara H, Ishihama A. Genomic SELEX Screening of Regulatory Targets of *Escherichia coli* Transcription Factors. *Methods Mol Biol.* 2018;1837: 49–69.
- 1755            29. Belliveau NM, Barnes SL, Ireland WT, Jones DL, Sweredoski MJ, Moradian A, et al. Systematic approach for dissecting the molecular mechanisms of transcriptional regulation in bacteria. *Proc Natl Acad Sci U S A.* 2018;115: E4796–E4805.

- 1760 30. Gao Y, Yurkovich JT, Seo SW, Kabimoldayev I, Dräger A, Chen K, et al. Systematic discovery of uncharacterized transcription factors in *Escherichia coli* K-12 MG1655. *Nucleic Acids Res.* 2018;46: 10682–10696.
- 1765 31. Sastry AV, Gao Y, Szubin R, Hefner Y, Xu S, Kim D, et al. The *Escherichia coli* transcriptome mostly consists of independently regulated modules. *Nat Commun.* 2019;10: 5536.
- 1765 32. Wu CH, Apweiler R, Bairoch A, Natale DA, Barker WC, Boeckmann B, et al. The Universal Protein Resource (UniProt): an expanding universe of protein information. *Nucleic Acids Res.* 2006;34: D187–91.
- 1770 33. Elemento O, Slonim N, Tavazoie S. A Universal Framework for Regulatory Element Discovery across All Genomes and Data Types. *Molecular Cell.* 2007. pp. 337–350. doi:10.1016/j.molcel.2007.09.027
- 1770 34. Gupta S, Stamatoyannopoulos JA, Bailey TL, Noble WS. Quantifying similarity between motifs. *Genome Biol.* 2007;8: R24.
- 1775 35. Goodarzi H, Elemento O, Tavazoie S. Revealing global regulatory perturbations across human cancers. *Mol Cell.* 2009;36: 900–911.
- 1775 36. Scholz SA, Diao R, Wolfe MB, Fivenson EM, Lin XN, Freddolino PL. High-Resolution Mapping of the *Escherichia coli* Chromosome Reveals Positions of High and Low Transcription. *Cell Syst.* 2019;8: 212–225.e9.
- 1780 37. Buenrostro JD, Wu B, Chang HY, Greenleaf WJ. ATAC-seq: A Method for Assaying Chromatin Accessibility Genome-Wide. *Curr Protoc Mol Biol.* 2015;109: 21.29.1–9.
- 1780 38. Whitfield CR, Wardle SJ, Haniford DB. The global bacterial regulator H-NS promotes transpososome formation and transposition in the Tn5 system. *Nucleic Acids Res.* 2009;37: 309–321.
- 1785 39. Tavazoie S, Church GM. Quantitative whole-genome analysis of DNA-protein interactions by in vivo methylase protection in *E. coli*. *Nat Biotechnol.* 1998;16: 566–571.
- 1785 40. Navarre WW, McClelland M, Libby SJ, Fang FC. Silencing of xenogeneic DNA by H-NS-facilitation of lateral gene transfer in bacteria by a defense system that recognizes foreign DNA. *Genes Dev.* 2007;21: 1456–1471.
- 1790 41. Navarre WW, Porwollik S, Wang Y, McClelland M, Rosen H, Libby SJ, et al. Selective silencing of foreign DNA with low GC content by the H-NS protein in *Salmonella*. *Science.* 2006;313: 236–238.
- 1790 42. Kahramanoglou C, Seshasayee ASN, Prieto AI, Ibberson D, Schmidt S, Zimmermann J, et al. Direct and indirect effects of H-NS and Fis on global gene expression control in *Escherichia coli*. *Nucleic Acids Research.* 2011. pp. 2073–2091. doi:10.1093/nar/gkq934
- 1795 43. Ling G, Waxman DJ. DNase I Digestion of Isolated Nuclei for Genome-Wide Mapping of DNase Hypersensitivity Sites in Chromatin. *Methods in Molecular Biology.* 2013. pp. 21–33. doi:10.1007/978-1-62703-284-1\_3
44. Mieczkowski J, Cook A, Bowman SK, Mueller B, Alver BH, Kundu S, et al. MNase titration



- reveals differences between nucleosome occupancy and chromatin accessibility. *Nat Commun.* 2016;7: 11485.
- 1800 45. Melfi MD, Lasker K, Zhou X, Shapiro L. ATAC-seq reveals megabase-scale domains of a bacterial nucleoid. *bioRxiv.* 2021. p. 2021.01.09.426053. doi:10.1101/2021.01.09.426053
46. Al-Bassam MM, Moyne O, Chapin N, Zengler K. Nucleoid openness profiling links bacterial genome structure to phenotype. *bioRxiv.* 2020. p. 2020.05.07.082990. doi:10.1101/2020.05.07.082990
- 1805 47. Freddolino P, Goss TJ, Amemiya HM, Tavazoie S. Dynamic landscape of protein occupancy across the *Escherichia coli* chromosome. *bioRxiv.* 2020. Available: <https://www.biorxiv.org/content/10.1101/2020.01.29.924811v1.abstract>
48. Fang X, Sastry A, Mih N, Kim D, Tan J, Yurkovich JT, et al. Global transcriptional regulatory network for *Escherichia coli* robustly connects gene expression to transcription factor activities. *Proc Natl Acad Sci U S A.* 2017;114: 10286–10291.
- 1810 49. Singh SS, Singh N, Bonocora RP, Fitzgerald DM, Wade JT, Grainger DC. Widespread suppression of intragenic transcription initiation by H-NS. *Genes Dev.* 2014;28: 214–219.
50. Kotlajich MV, Hron DR, Boudreau BA, Sun Z, Lyubchenko YL, Landick R. Bridged filaments of histone-like nucleoid structuring protein pause RNA polymerase and aid termination in bacteria. *Elife.* 2015;4. doi:10.7554/eLife.04970
- 1815 51. Landick R, Wade JT, Grainger DC. H-NS and RNA polymerase: a love--hate relationship? *Curr Opin Microbiol.* 2015;24: 53–59.
52. Atlung T, Ingmer H. H-NS: a modulator of environmentally regulated gene expression. *Mol Microbiol.* 1997;24: 7–17.
- 1820 53. Ono S, Goldberg MD, Olsson T, Esposito D, Hinton JCD, Ladbury JE. H-NS is a part of a thermally controlled mechanism for bacterial gene regulation. *Biochem J.* 2005;391: 203–213.
54. Karp PD, Weaver D, Paley S, Fulcher C, Kubo A, Kothari A, et al. The EcoCyc Database. *EcoSal Plus.* 2014;6. doi:10.1128/ecosalplus.ESP-0009-2013
55. Kass RE, Raftery AE. Bayes Factors. *J Am Stat Assoc.* 1995;90: 773–795.
- 1825 56. Freddolino PL, Amini S, Tavazoie S. Newly identified genetic variations in common *Escherichia coli* MG1655 stock cultures. *J Bacteriol.* 2012;194: 303–306.
57. Ausubel FM. *Current Protocols in Molecular Biology.* John Wiley & Sons; 1998.
- 1830 58. Baba T, Ara T, Hasegawa M, Takai Y, Okumura Y, Baba M, et al. Construction of *Escherichia coli* K-12 in-frame, single-gene knockout mutants: the Keio collection. *Mol Syst Biol.* 2006;2: 2006.0008.
59. Cherepanov PP, Wackernagel W. Gene disruption in *Escherichia coli*: TcR and KmR cassettes with the option of Flp-catalyzed excision of the antibiotic-resistance determinant. *Gene.* 1995;158: 9–14.

- 1835 60. Huisman O, D'Ari R. An inducible DNA replication–cell division coupling mechanism in *E. coli*. *Nature*. 1981;290: 797–799.
61. Huisman O, D'Ari R, Gottesman S. Cell-division control in *Escherichia coli*: specific induction of the SOS function SfiA protein is sufficient to block septation. *Proc Natl Acad Sci U S A*. 1984;81: 4490–4494.
- 1840 62. Gibson DG, Young L, Chuang R-Y, Venter JC, Hutchison CA 3rd, Smith HO. Enzymatic assembly of DNA molecules up to several hundred kilobases. *Nat Methods*. 2009;6: 343–345.
63. Neidhardt FC, Bloch PL, Smith DF. Culture medium for enterobacteria. *J Bacteriol*. 1974;119: 736–747.
- 1845 64. Mooney RA, Davis SE, Peters JM, Rowland JL, Ansari AZ, Landick R. Regulator trafficking on bacterial transcription units in vivo. *Mol Cell*. 2009;33: 97–108.
65. Tange O, Others. Gnu parallel—the command-line power tool. *The USENIX Magazine*. 2011;36: 42–47.
66. Martin M. Cutadapt removes adapter sequences from high-throughput sequencing reads. *EMBnet.journal*. 2011;17: 10–12.
- 1850 67. Bolger AM, Lohse M, Usadel B. Trimmomatic: a flexible trimmer for Illumina sequence data. *Bioinformatics*. 2014;30: 2114–2120.
68. Andrews S, Others. FastQC: a quality control tool for high throughput sequence data. Babraham Bioinformatics, Babraham Institute, Cambridge, United Kingdom; 2010.
- 1855 69. Ewels P, Magnusson M, Lundin S, Käller M. MultiQC: summarize analysis results for multiple tools and samples in a single report. *Bioinformatics*. 2016;32: 3047–3048.
70. Du P, Kibbe WA, Lin SM. Improved peak detection in mass spectrum by incorporating continuous wavelet transform-based pattern matching. *Bioinformatics*. 2006;22: 2059–2065.
- 1860 71. Slonim N, Atwal GS, Tkacik G, Bialek W. Information-based clustering. *Proc Natl Acad Sci U S A*. 2005;102: 18297–18302.
72. Pimentel H, Bray NL, Puente S, Melsted P, Pachter L. Differential analysis of RNA-seq incorporating quantification uncertainty. *Nat Methods*. 2017;14: 687–690.
73. Quinlan AR. BEDTools: the Swiss-army tool for genome feature analysis. *Curr Protoc Bioinformatics*. 2014;47: 11–12.
- 1865 74. Grant CE, Bailey TL, Noble WS. FIMO: scanning for occurrences of a given motif. *Bioinformatics*. 2011;27: 1017–1018.
75. Pachkov M, Balwierz PJ, Arnold P, Ozonov E, van Nimwegen E. SwissRegulon, a database of genome-wide annotations of regulatory sites: recent updates. *Nucleic Acids Res*. 2013;41: D214–20.
- 1870 76. Elemento O, Tavazoie S. Fast and systematic genome-wide discovery of conserved

- regulatory elements using a non-alignment based approach. *Genome Biol.* 2005;6: R18.
77. Castro-Mondragon JA, Jaeger S, Thieffry D, Thomas-Chollier M, van Helden J. RSAT matrix-clustering: dynamic exploration and redundancy reduction of transcription factor binding motif collections. *Nucleic Acids Res.* 2017;45: e119.
- 1875 78. Kawano M, Aravind áL, Storz G. An antisense RNA controls synthesis of an SOS-induced toxin evolved from an antitoxin. *Mol Microbiol.* 2007;64: 738–754.
79. Thibodeau SA, Fang R, Joung JK. High-throughput beta-galactosidase assay for bacterial cell-based reporter systems. *Biotechniques.* 2004;36: 410–415.
- 1880 80. Bürkner P-C. brms: An R Package for Bayesian Multilevel Models Using Stan. *Journal of Statistical Software, Articles.* 2017;80: 1–28.
81. Herring CD, Raffaella M, Allen TE, Kanin EI, Landick R, Ansari AZ, et al. Immobilization of *Escherichia coli* RNA polymerase and location of binding sites by use of chromatin immunoprecipitation and microarrays. *J Bacteriol.* 2005;187: 6166–6174.
- 1885 82. Campbell EA, Korzheva N, Mustaev A, Murakami K, Nair S, Goldfarb A, et al. Structural mechanism for rifampicin inhibition of bacterial rna polymerase. *Cell.* 2001;104: 901–912.
83. Cabrera JE, Cagliero C, Quan S, Squires CL, Jin DJ. Active transcription of rRNA operons condenses the nucleoid in *Escherichia coli*: examining the effect of transcription on nucleoid structure in the absence of transertion. *J Bacteriol.* 2009;191: 4180–4185.
- 1890 84. Pettijohn DE, Hecht R. RNA molecules bound to the folded bacterial genome stabilize DNA folds and segregate domains of supercoiling. *Cold Spring Harb Symp Quant Biol.* 1974;38: 31–41.
85. Cabrera JE, Jin DJ. The distribution of RNA polymerase in *Escherichia coli* is dynamic and sensitive to environmental cues. *Mol Microbiol.* 2003;50: 1493–1505.
- 1895 86. Dworsky P, Schaechter M. Effect of rifampin on the structure and membrane attachment of the nucleoid of *Escherichia coli*. *J Bacteriol.* 1973;116: 1364–1374.
87. Francetic O, Belin D, Badaut C, Pugsley AP. Expression of the endogenous type II secretion pathway in *Escherichia coli* leads to chitinase secretion. *EMBO J.* 2000;19: 6697–6703.
- 1900 88. Breunig MM, Kriegel H-P, Ng RT, Sander J. LOF: identifying density-based local outliers. *Proceedings of the 2000 ACM SIGMOD international conference on Management of data.* New York, NY, USA: Association for Computing Machinery; 2000. pp. 93–104.
89. Pedregosa F, Varoquaux G, Gramfort A, Michel V, Thirion B, Grisel O, et al. Scikit-learn: Machine learning in Python. *the Journal of machine Learning research.* 2011;12: 2825–2830.
- 1905 90. Benjamini Y, Hochberg Y. Controlling the False Discovery Rate: A Practical and Powerful Approach to Multiple Testing. *J R Stat Soc Series B Stat Methodol.* 1995;57: 289–300.
91. Lal A, Dhar A, Trostel A, Kouzine F, Seshasayee ASN, Adhya S. Genome scale patterns of supercoiling in a bacterial chromosome. *Nat Commun.* 2016;7: 11055.

- 1910 92. Prieto AI, Kahramanoglou C, Ali RM, Fraser GM, Seshasayee ASN, Luscombe NM. Genomic analysis of DNA binding and gene regulation by homologous nucleoid-associated proteins IHF and HU in *Escherichia coli* K12. *Nucleic Acids Res.* 2012;40: 3524–3537.
93. Joshi MC, Magnan D, Montminy TP, Lies M, Stepankiw N, Bates D. Regulation of sister chromosome cohesion by the replication fork tracking protein SeqA. *PLoS Genet.* 2013;9: e1003673.
- 1915 94. Chiu T-P, Comoglio F, Zhou T, Yang L, Paro R, Rohs R. DNASHapeR: an R/Bioconductor package for DNA shape prediction and feature encoding. *Bioinformatics.* 2016;32: 1211–1213.